

POLITECNICO DI TORINO

**Master's Degree
in Automotive Engineering**

Master's Thesis

Feasibility study of Directed Energy Deposition for stainless steel sheet reinforcement



**Politecnico
di Torino**

Thesis supervisors

Prof.ssa Atzeni Eleonora

Prof. Salmi Alessandro

Prof. Piscopo Gabriele

Candidate

Giuliano Stefano

Academic year 2022-2023

Abstract

The objective of this study is to reinforce a thin sheet of AISI 304 stainless steel by means of a series of depositions of AISI 316L stainless steel powder using Directed Energy Deposition. The experiment is divided into different phases: at first the right process parameters have to be correctly set up; secondly, the different test pieces have to be produced; at last, all the samples have to be tested in the bending machine and analysed under the microscope to understand the differences among the various geometries of deposition considered. Results suggest that the use of this production technology can be a viable solution to increase the bending stiffness of a thin sheet of stainless steel.

Index

1. Introduction.....	7
2. Directed Energy Deposition.....	9
2.1 Process parameters.....	11
2.2 Deposition patterns.....	13
2.3 Microstructure.....	15
2.4 Melt pool	17
2.5 DED component defects.....	19
2.5.1 Porosity	19
2.5.2 Cracking, delamination and swelling	21
2.5.3 Residual stresses	23
2.6 Oxidation	24
2.7 Corrosion resistance.....	26
2.8 Materials.....	30
3. Experiment set-up.....	32
3.1 DED machine	32
3.2 The study.....	33
3.3 Preliminary test	34
3.4 Bend Test machine.....	37
3.5 Microscope.....	40
3.6 Experiment setup	41
4 Analysis.....	45
4.1 Photo analysis.....	45
4.1.1 Vertical Depositions.....	46
4.1.2 Horizontal Depositions.....	47
4.1.3 Diagonal Deposition.....	49
4.2 Bend test	50
4.2.1 Blank sheet bend test	54
4.2.3 Vertical depositions bend test	56
4.2.4 Horizontal depositions bend test.....	60
4.2.5 Diagonal depositions bend test	64
4.2.6 Global comparison	67

5. Conclusions	70
6. Bibliography	72

List of Figures

Figure 1 Evolution of additive manufacturing [5]	7
Figure 2 General directed energy deposition machine [7]	9
Figure 3 List of the various parameters that can affect the metal layer deposition process [27]	11
Figure 4 Powder injection point "A", (a) ahead, (b) in-line with, and (c) behind the laser spot centre "O" [8]	12
Figure 5 Possible deposition strategies, (a) linear, (b) zig-zag, (c) chessboard, (d) contour [10]	14
Figure 6 SEM powder morphology of stainless steel powder produced by: (a) gas atomization, (b) water atomization [28]	16
Figure 7 Melt pool and heat affected zone representation [29]	17
Figure 8 Heat transfer processes [30]	18
Figure 9 Different kinds of porosities observed with light optical microscopy [31]	19
Figure 10 Trend of porosity percentage as a function of scan speed and energy density at constant laser power [20]	21
Figure 11 Delamination [31]	22
Figure 12 Residual stresses formation model: (a) heating, (b) cooling [32]	23
Figure 13 Non-metallic inclusions mean radius as a function of cooling rate for a conventional casting production process and a Laser Metal Deposition process [21]	26
Figure 14 General stainless steel anodic polarization curve [26]	27
Figure 15 Pitting corrosion on stainless steel [26]	29
Figure 16 Pitting corrosion mechanism [26]	29
Figure 17 Microstructure of a 316L steel using DED: fine grain structure (a), islands of elongated grains (b and c) and finer grains (d) [35]	31
Figure 18 Optomec powder feeder	32
Figure 19 Deposition tests to determine the best DED parameters pre-sets.	36
Figure 20 Detailed shot of the bend test machine. The metal bracket used to align the test piece is clearly visible.	38
Figure 21 Bend angle test drawing [36]	38
Figure 22 Leica S9i microscope. Under the light is the deposition test steel sheet	40
Figure 23 Vertical separated (left) and merged (right) deposition tracks test pieces.	42
Figure 25 Horizontal separated (left) and merged (right) deposition tracks test pieces.	42
Figure 27 Diagonal separated (left) and merged (right) deposition tracks test pieces	43
Figure 29 A test piece inside the DED machine after the deposition	44
Figure 30 All the different test pieces geometries	45
Figure 31 Vertical merged deposition microscope close-up	46
Figure 32 Vertical separated deposition microscope close-up	46
Figure 33 Horizontal merged deposition microscope close-up	47
Figure 34 Vertical separated deposition microscope close-up	48
Figure 35 Diagonal merged deposition microscope close-up	49
Figure 36 Vertical separated deposition microscope close-up	49
Figure 37 Comparison between the same geometry placed in the bend test machine with the depositions on the compression side or on the tension side.	51
Figure 38 First millimetre of travel of the former, plot extrapolated from Figure (37).	52
Figure 39 38 Second half of travel of the former, plot extrapolated from Figure (37).	53
Figure 40 Comparison of the results of the five blanks bend test	54
Figure 41 Blank test piece after the bend test. Picture taken with the microscope.	55
Figure 42 Comparison of the results of the five vertical separated depositions bend test.	56
Figure 43 Vertical separated deposition test piece after the bend test. Picture taken with the microscope.	57
Figure 44 Comparison of the results of the five vertical merged depositions bend test.	57
Figure 45 Vertical merged deposition test piece after the bend test. Picture taken with the microscope.	58
Figure 46 Comparison of the results of the five horizontal separated depositions bend test	60

<i>Figure 47 Horizontal separated deposition test piece after the bend test. Picture taken with the microscope.</i>	61
<i>Figure 48 Horizontal merged deposition bend test. The moment of the slip of the test piece is clearly visible.</i>	61
<i>Figure 49 Horizontal merged deposition test piece after the bend test. Picture taken with the microscope.</i>	62
<i>Figure 50 Comparison of the results of the five diagonal separated depositions bend test</i>	64
<i>Figure 51 Diagonal separated deposition test piece after the bend test. Picture taken with the microscope.</i>	64
<i>Figure 52 Comparison of the results of the five diagonal merged depositions bend test.</i>	65
<i>Figure 53 Diagonal merged deposition test piece after the bend test. Picture taken with the microscope.</i>	65
<i>Figure 54 Comparison of the bend test among all the different deposition geometries and the blank.</i>	67
<i>Figure 55 Comparison of the bend test among all the different deposition geometries and the blank. The horizontal merged deposition is included.</i>	69

List of Tables

<i>Table 1 AISI 316L composition [34]</i>	30
<i>Table 2 Laserdyne 430 specifications [35]</i>	32
<i>Table 3 Different combinations of the three main parameters for the deposition tests</i>	35
<i>Table 4 Bend angle as a function of the distance travelled by the former, according to equations (1) through (4)</i>	39
<i>Table 5 Bend test results for the blank test pieces.</i>	56
<i>Table 6 Bend test results for the vertical separated deposition test pieces.</i>	59
<i>Table 7 Bend test results for the vertical merged deposition test pieces.</i>	60
<i>Table 8 Bend test results for the horizontal separated deposition test pieces.</i>	63
<i>Table 9 Bend test results for the diagonal separated deposition test pieces.</i>	66
<i>Table 10 Bend test results for the diagonal merged deposition test pieces.</i>	67
<i>Table 11 Comparison of the average results of the different bend tests.</i>	68

1. Introduction

The term additive manufacturing (AM), or as it is more generally known, albeit improperly, 3D printing, is related to a wide variety of production methodologies and technologies. What differentiates AM from traditional subtractive manufacturing is the way the products are built: layer by layer, starting from a 3D CAD representation, without the need for any kind of tool [2]. The origins of this new manufacturing method are to be found in the 80's, in particular in the development of the stereolithography, where a plastic object can be obtained from a photosensitive polymer resin thanks to the layer-by-layer polymerization triggered by UV light focused using a system of mirrors. SLA-1 (StereoLithography Apparatus) was the first commercially available additive manufacturing system, debuting in 1987 [3]. Technology advanced to the point when in the 90's it was possible to produce metal parts using AM. In 1998 Optomec commercialized the first dedicated AM system for Directed Energy Deposition (DED), using powder feed laser energy deposition technology [4].

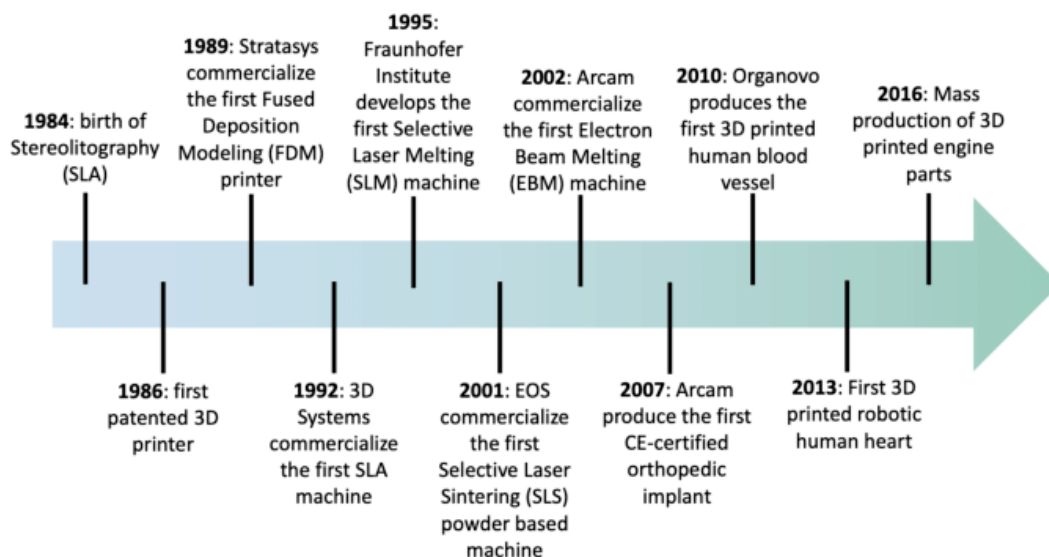


Figure 1 Evolution of additive manufacturing [5]

From this point on, this new manufacturing method quickly evolved until today, where it is no more used only for rapid prototyping but it's mature enough so that finished components can be obtained, and in a variety of shapes impossible to replicate with conventional manufacturing means.

In 2015, ISO (International Organization for Standardization) published, together with the ASTM (American Society for Testing and Materials) committee F42, a standard regarding additive manufacturing, later revised in 2021 under the name ISO/ASTM 52900:2021. This document individuates different AM technologies, organizing them in seven macro-categories [6]:

- Material extrusion: “the material is selectively dispensed through a nozzle or orifice”;
- Material jetting: “droplets of build material are selectively deposited”;
- Binder jetting: “a liquid bonding agent is selectively deposited to join powder material”;
- Sheet lamination: “material sheets are bonded to form an object”;
- Vat photopolymerization: “liquid photopolymer in a vat is selectively cured by light-activated polymerization”;
- Powder bed fusion: “thermal energy selectively fuses regions of a powder bed”;
- Directed energy deposition: “focused thermal energy is used to fuse materials by melting as the material is deposited”;

2. Directed Energy Deposition

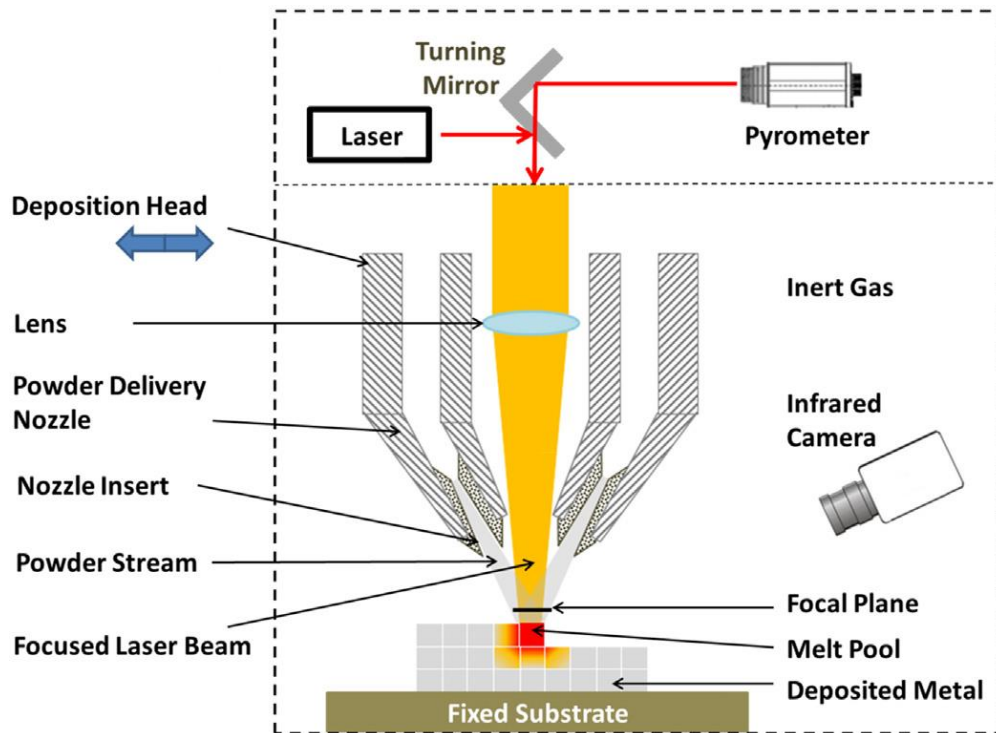


Figure 2 General directed energy deposition machine [7]

Directed Energy Deposition is one of the AM processes suitable to be implemented for the production of metal components. Metal Additive Manufacturing systems can mainly be divided into two categories: powder bed systems or powder/wire feed systems. In the former the building material, in the form of a fine powder, is spread across the building platform area by a blade or a recoater, and the energy to melt it in the desired shape is provided by a laser beam or an electron beam that moves on the plane following the CAD instructions. When a layer is completed, new powder is spread and the process repeats until completion of the piece. In the latter, instead, the building material is fed directly in the melt pool created by the energy source, as it moves along the current layer, that melts it and makes it bond to the substrate. DED allows to obtain fully dense objects, as well as bigger building volumes [1].

Powders are fed into inside the melt pool by means of a carrier gas, passing through a system of nozzles. As this happens the energy source, the laser in the case of the equipment used for this thesis, has to be correctly configured in order to have the right conditions to melt the incoming powder without thermally affect too much the underlying layers. Due to the high temperatures needed to melt the metal powder an inert gas is blown in order to shield as much as possible the new layer from oxidation. Argon is frequently used and resulting concentration of oxygen in the component must not exceed 2-3 ppm [7].

Lasers can be of different types, but the most common are fibre laser, the key point is that the energy is high enough and the wavelength compatible with the material the component is made of, not to cause a lowering in the efficiency and an increase of the costs.

Powder characterization is very important for the mechanical properties of the finished component as these are impacted by chemical composition, porosity and morphology of the powder used. The most frequently used powders are obtained by gas atomization. This process allows to obtain spherical particles by disrupting the stream of liquid metal by a high velocity gas, being it air, nitrogen, argon or helium. The use of these powders, with a granulometry between 10 and 100 μm [6], allows to obtain a better powder flow and a lower end material porosity as the inert gas is not trapped as much as it would with a more irregular powder. Not all kinds of material can be used: powders with very high thermal conductivity or reflectance are not suitable for this application as they could reflect the laser causing damages to the equipment. Powder feed rate is variable depending on the nozzle diameter and the other process parameters, but usually is between 1 and 10 g/min, with the time between a layer deposition and the next lower than 1000 s [6].

2.1 Process parameters

There are a total of 19 process parameters for DED [27] and the microstructure of the component manufactured is dependent on those as the thermal history the material faces changes, as well as the shape of the melt pool and thus the thermal gradients present.

Material	Laser	Product	Process	Environment
Density, ρ	Beam Diameter at Focus, d_F	Height of Deposit, h_D	Delivered Mass Flow Rate, \dot{m}_{del}	Gravity, g
Thermal Conductivity, k	Power, P	Width of Deposit, w	Deposited Mass Flow Rate, \dot{m}_{dep}	
Solidification Time, t_s			Energy Loss to Environment, \dot{E}_l	
Viscosity, μ			Translation Speed, v_s	
Heat Capacity, c_p			Powder Size, d_p	
Surface Tension, σ			Initial Powder Temperature, T_i	
Melting Energy, \dot{E}_m			Powder Stream Speed, v_p	

Figure 3 List of the various parameters that can affect the metal layer deposition process [27]

One of the most influential parameters is the laser power, generally in the range between 100 and 5000 W [7], as it determines the number of defects in the finished component. Also important is the relative speed between the deposition head and the substrate, as well as the powder flow and the positioning of the nozzle with respect to the laser, that are now typically coaxial. Powders can be injected in front, in line or behind the laser focusing point and this changes the amount of powder directly flowing inside the melt pool and the portion of it that hits the layer already formed, bouncing off and reducing the efficiency of the powder utilization [7].

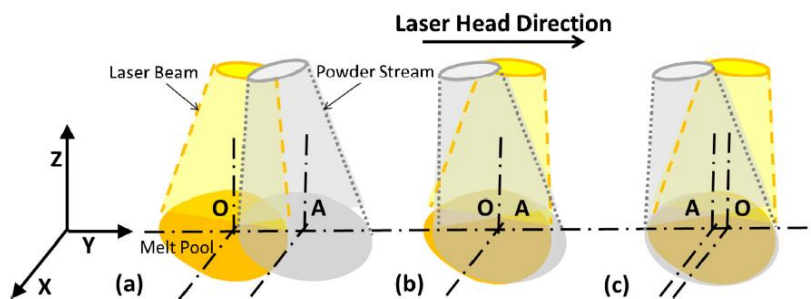


Figure 4 Powder injection point "A", (a) ahead, (b) in-line with, and (c) behind the laser spot centre "O" [8]

By positioning the powder nozzle slightly behind the laser the most portion of incoming powders will be directed inside the melt pool. [8] Another parameter influencing the amount of powders flowing inside the melt pool is the behaviour of the powders with the shielding gas: the higher the gas velocity the higher the powder flow, but a speed too high would end in the powders bouncing off the melt pool instead of being trapped inside, thus, the real amount of powder hitting the melt pool is lower.

The scan speed is proportional to the laser power used: if the laser is very energetic the scan speed can be increased, still obtaining a big enough melt pool. If, instead, the laser is less powerful the scan speed has to be lowered, or the melt pool dimensions would diminish.

The hatching distance, that is the distance between two adjacent melt pools, is an important parameter to define as it has a direct effect on the overlapping of the tracks. Porosities in the end component are linked to these parameters: increasing the hatching distance the porosity increases linearly because the overlapping lowers so some portions of the powder may not melt properly [9].

2.2 Deposition patterns

The deposition of the material happens in a similar way as in milling operations using CAM software. Although the principle behind the choice of path is similar (removing layers of material is not that different from adding them) there are a lot of new variables playing a role in the DED process towards the mechanical properties of the finished product: from the overlapping between adjacent beads to the laser spot size and the bead cross section. The selection of proper paths in AM is still of primary importance, not only to minimize the fabrication time but also to achieve good material properties [10].

A possible strategy for the deposition pattern is that of dividing every layer in two zones: a contour made with a single, uninterrupted pass, to give the piece a better dimensional accuracy and surface finish, and a fill realized later in a second pass with different strategies to choose from. If the surface finish of the component produced is of interest, the contour may be done as the last step. There's not a clear "best solution", but to get the lowest distortions of the component at the end of the manufacturing is important to keep the temperatures in check, trying not to heat up too much single regions of the layer that would warp due to the thermal distribution. Kandice S. B. Ribeiro et al. [10] found in their study that a contour strategy

(helical-like) gives the best results in terms of face distortion as the heat transfer over the workpiece trajectory is better uniformly distributed compared to other deposition strategies. Heat is initially put at the centre of the layer, then uniformly distributed to the preceding layer and to the shielding gas. This strategy also showed a density closer to the conventional annealed material used (SS 316L) than with different deposition strategies, as well as the closest hardness values [10].

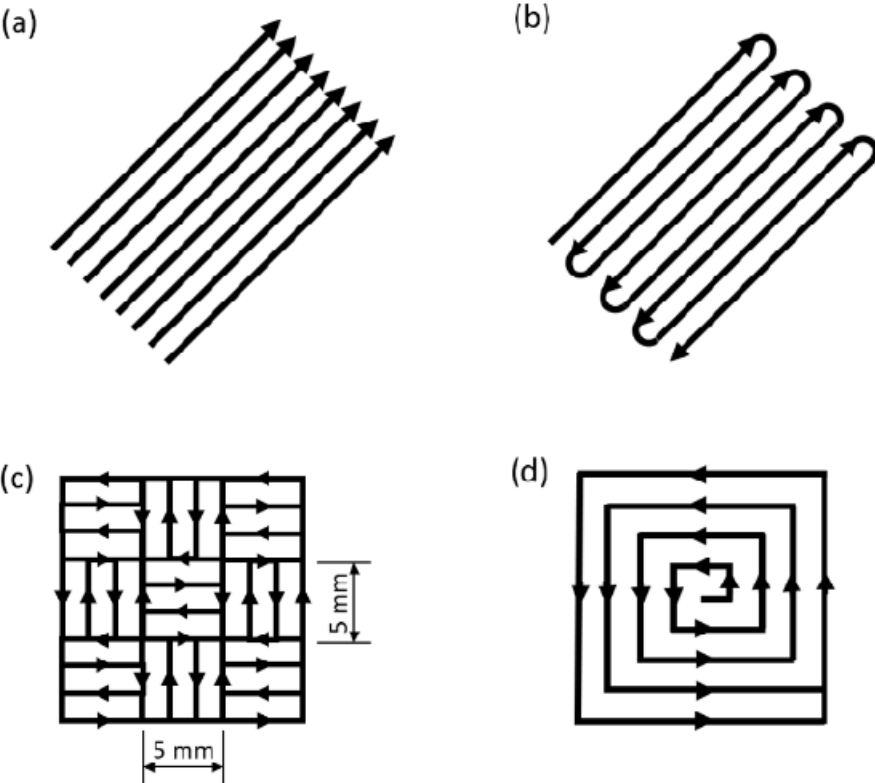


Figure 5 Possible deposition strategies, (a) linear, (b) zig-zag, (c) chessboard, (d) contour [10]

2.3 Microstructure

As already stated, the microstructure of a component realized with additive manufacturing technologies is highly dependent on the process parameters chosen, like the laser power or the scanning pattern. What essentially happens during a DED process is a rapid melting of the powder followed by a quick solidification of the melting pool, as the amount of material involved is low and the laser sufficiently powerful. This process leads to a component with a very fine microstructure, up to 10 times finer than the one that could be obtained by a conventional casting process [11]. Shamsaei et al. [7] defined two variables in their study, G and R , both tied to the different microstructures obtainable. They are defined as:

$$R = \frac{\text{cooling rate}}{\text{thermal gradient}} = \text{local solidification rates within the melt pool}$$

G =temperature gradient at the solid-liquid interface

Two critical solidification parameters are the cooling rate, given by the product $G * R$, that influences the microstructure dimensions, and the ratio G/R , that affects the solid-liquid interface shape. Different values for these variables lead to the formation of different structure morphologies within the produced component: equiaxed (isotropic grain morphology), columnar (elongated grain morphology) or a combination of the two. Increasing the cooling rate, $G * R$ leads to a finer microstructure, increasing the solidification rate promotes the transition from columnar to equiaxed grain morphologies, while the tendency for the formation of a columnar structure is increased by increasing the ratio G/R . Instead, decreasing this ratio leads to the formation of mainly equiaxed structures. The optimal values for the variables G and R are also dependant on the part geometry, the material property, environmental and machine conditions and other process parameters [11].

The final component microstructure is also influenced by the kind of powder utilized. Water-atomized powders are a viable alternative to gas-atomized ones in the DED process, producing smoother walls once deposited, with a finer and more textured microstructure and slightly thicker oxide-rich surface layer. Deposition rates and powder efficiencies are, however, considerably lower. These differences in performance between powder types can be explained by an higher oxygen concentration in the water-atomized powder and an increased energy absorption due to the more irregular shape of this kind of powder [12].

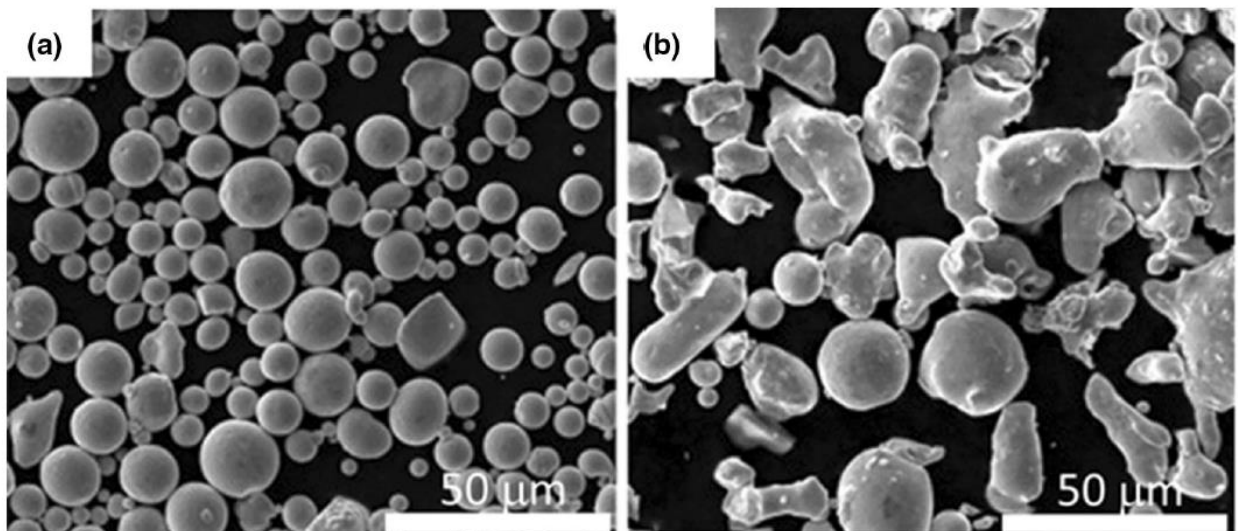


Figure 6 SEM powder morphology of stainless steel powder produced by: (a) gas atomization, (b) water atomization [28]

2.4 Melt pool

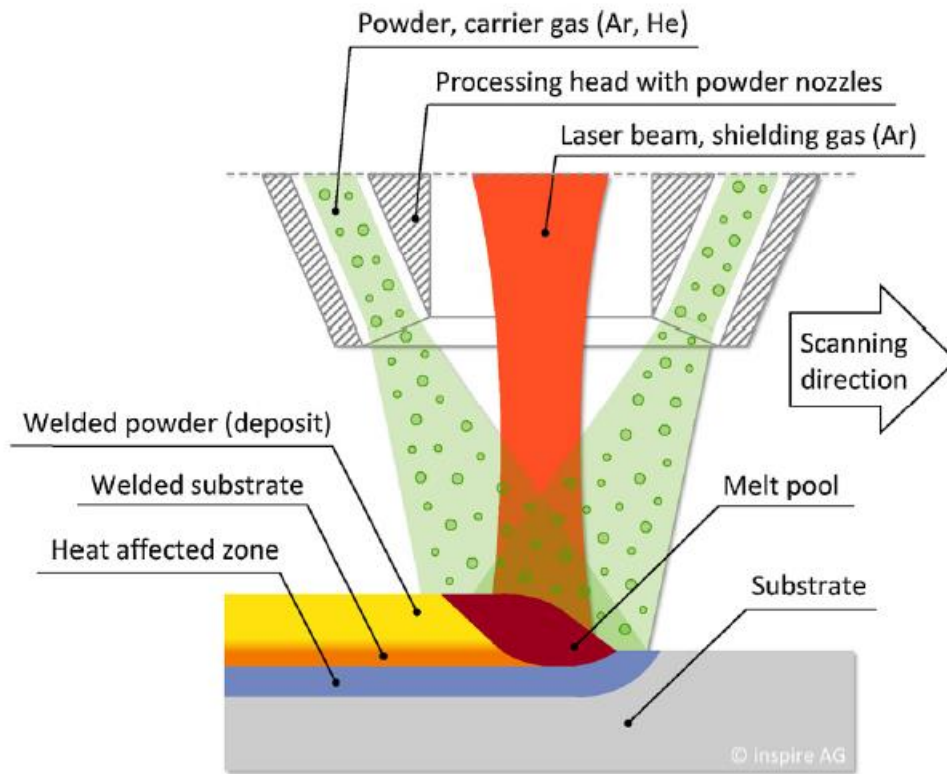


Figure 7 Melt pool and heat affected zone representation [29]

The melt pool is the region of space where the laser hits the material, giving rise to a heat transfer that's high enough to make the powder change phase. It has a characteristic hemispherical drop shape, moving at the laser scanning speed on the substrate. Melt pool morphology and temperature are in part responsible for dimensional tolerances, microstructure and eventual residual stresses in the component once it is cooling down because the melt pool itself is the origin of the additive manufactured component. The melt pool is not that different from the one generated by a laser welding, but the continuous flow of powders make the temperature analysis more difficult and give rise to a small amount of instability due to the

powder flow, with the small particles interfering with the laser, absorbing part of the energy that should reach the melt pool [6]. Finer powders allow to obtain a more stable melt pool, while more gross particles lead to an high instability of the surface of the melt pool non in contact with the substrate [13].

The melt pool is a region with a very high thermal gradient, especially close to the focusing point of the laser, where differences in temperature are emphasized by the phase transition of the powder that is melting. Close to the boundaries of the melt pool the gradients are less steep. These differences in temperature are due to the laser heat being transmitted by conduction to the surrounding material, giving rise to the heat affected zone (HAZ), a region of space where the metal microstructure and mechanical properties could be different due to the thermal history the material has been subjected to. By monitoring the cooling rate it is possible to control the component final microstructure and reduce to a minimum both distortions and residual stresses.

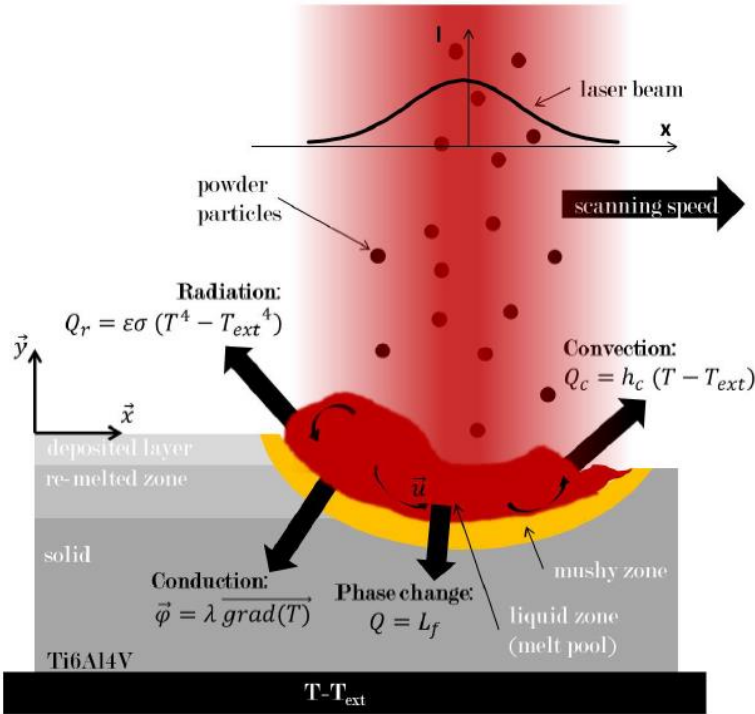


Figure 8 Heat transfer processes [30]

2.5 DED component defects

The optimization of the process parameters allows to keep at a minimum the various defects.

The most common ones are:

- Porosities,
- Cracking, delamination and swelling,
- Residual stresses

2.5.1 Porosity

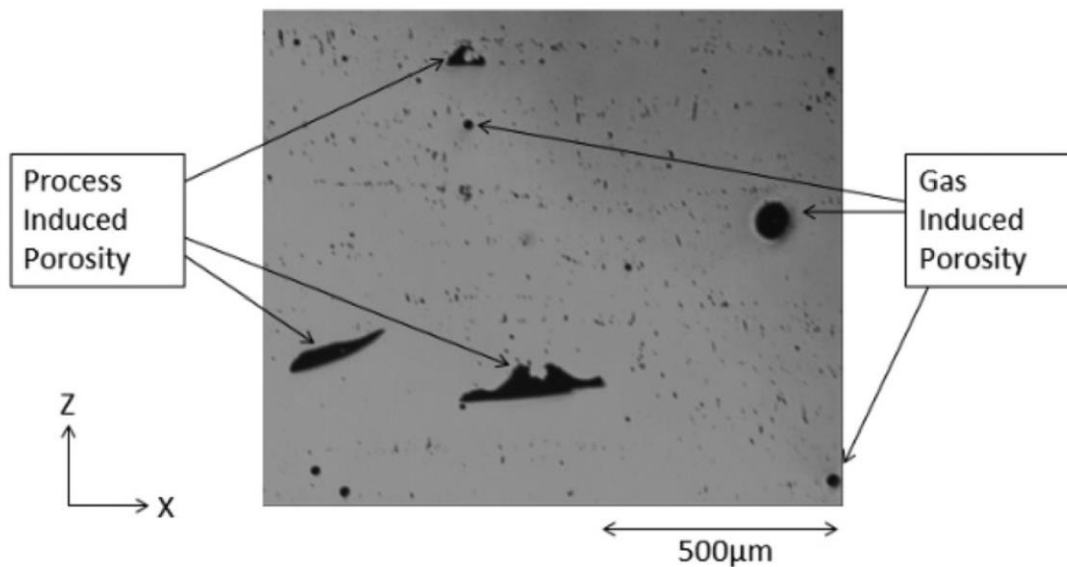


Figure 9 Different kinds of porosities observed with light optical microscopy [31]

Porosity is a common defect in metal parts produced with AM technologies. It can be powder induced, process induced or a result of the solidification process. During the powder atomization some gas pores may be created inside the powder feedstock and these spherical pores can be directly transferred to the additively manufactured component. More often, though, pores are a result of the process parameters chosen. These process induced porosities are formed when there's not enough energy applied by the laser to completely melt the powder or too much, resulting in spatter ejection. These kinds of pores usually appear of irregular shapes, coming in a variety of different sizes, from sub-micron to macroscopic.

When not enough power is supplied to a region of powder, lack of fusion can occur. Regions where this happens can be identified looking for un-melted powder particles inside or near the pore. On the contrary, when too much power is applied, the spatter ejection phenomenon can take place. This process is known as keyhole formation. The amount of porosities present is related to the scan speed and energy density at constant power, as can be seen in Figure (10). Experimental studies found out that porosities due to keyholing were increasing at high energy density, that is high power and low speed, a minimum for intermediate energy density levels and then another increase of porosities, this time due to incomplete melting, for lower energy

densities [20]. By optimizing the process parameters, process induced porosities can be reduced to values lower than 1% [14].

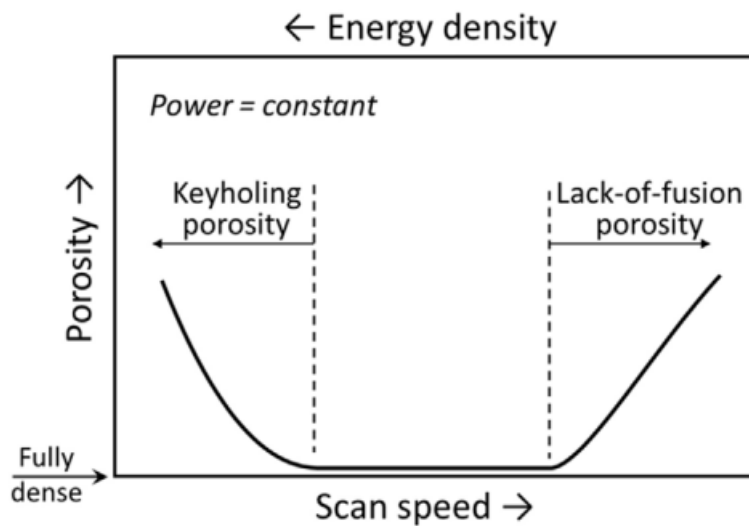


Figure 10 Trend of porosity percentage as a function of scan speed and energy density at constant laser power [20]

2.5.2 Cracking, delamination and swelling

The formation of these defects is closely related to the process temperature, with some macroscopic cracks due to the presence of porosities while cracking of the microstructure occurring during solidification or subsequent heating. A process temperature too high may lead to swelling.

Different mechanisms exist for which cracks form during AM processes [15]. Solidification cracking can occur in some cases if too much energy is applied during the AM process and is

due to the stresses caused by the interaction between solidified areas of the melt pool and areas that have yet to solidify. The higher energy applied leads to higher thermal gradients and this can explain the larger thermal stress required for solidification cracking. Grain boundary cracking is another kind of defect that nucleates and occurs along the grain boundaries of the metal material. The origins of this kind of cracking depends on the material type and rely to the formation and dissolution of precipitate phases and to the morphology of the grain boundary. It is not a given that the process parameters that are required to minimize the process induced porosities are the same that also minimize the likelihood of the formation of cracks. Moreover, some cracks are macroscopic defects that can nucleate because of other macroscopic defects such as delamination, not even related to excessive heating [15].

Delamination is the phenomenon for which two adjacent layer within the component separate as a consequence of incomplete melting of powders or insufficient re-melting of the underlying solid substrate. This kind of defect has macroscopic effects and cannot be repaired by any post-processing action. To reduce its occurrence substrate heating has proven successful [16].



Figure 11 Delamination [31]

Swelling is the rise of solid material above the plane of powder distribution and melting and occurs due to surface tension effects related to the melt pool geometry [17]. Swelling could also happen because of the presence of porosities that locally lower the thermal conductivity, causing this defect on subsequent layer due to an unexpected thermal resistance [15].

2.5.3 Residual stresses

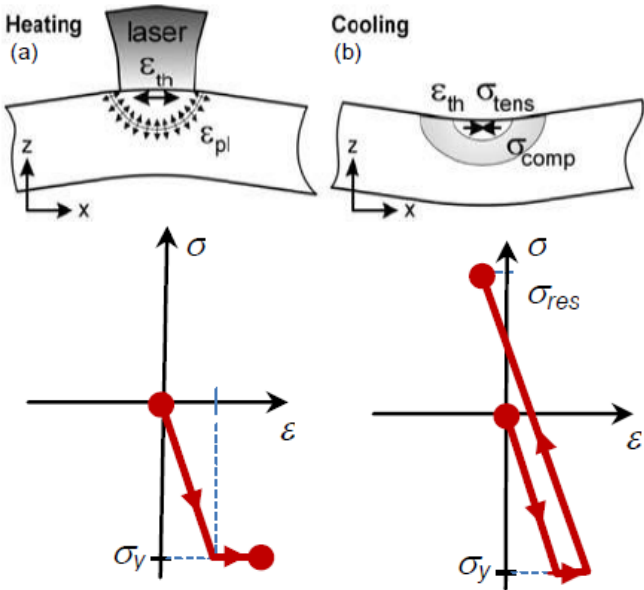


Figure 12 Residual stresses formation model: (a) heating, (b) cooling [32]

Residual stress is a stress within the material that persists even after the removal of a pre-existing stress. This kind of long lasting stresses are common in additively manufactured components due to the large thermal gradients these components are subjected to during the formation process. Mechanical properties may be negatively impacted, changes in the grain

structure may be encouraged and they can lead to geometrical distortions. When the residual stress overcomes the local material yield stress, plastic deformation may occur, while if the stresses are high enough to overcome even the local ultimate tensile strength of the material, cracking may occur. Macroscopic residual stresses in metal AM can be thermally introduced by either a differential heating of the solid or by a differential cooling during and after the solidification [18].

Xufei Lu et al. [19] studied ways to reduce the residual stresses in DED AM processes, that are usually compressive in the centre of the component produced, while are of tensile nature at the edge. The most of these residual stresses is due to the first layers being deposited onto a substrate still cold, thus resulting in very high temperature gradients. Substrate heating is a viable way to reduce the entity of this problem. Like in other fabrication processes, the rounding of sharp angles of the component is another recommended action to keep residual stresses at a minimum. Also using smaller substrate, even hollow ones where feasible, allows to obtain faster transients, with the substrate heating up quicker and thus reducing the stresses generated.

2.6 Oxidation

Temperatures during a DED process can reach in a very short time really high values in the melt pool, with peaks of 2300 K in the case of AISI 316 stainless steel [21]. Even if the material is subjected to these kind of temperature for a very brief time, less than a few seconds, this is enough for the molten metal in the melt pool to react with oxygen molecules, even in the presence of the shielding gas. As a result of this oxidation, non-metallic inclusions are formed

and finely dispersed inside the melt pool [22]. The presence of these inclusions is usually unwanted as they can deteriorate corrosion and fatigue properties and act as nucleation sites for crack during the life of the component. Despite these drawbacks, however, non metallic inclusions have recently attracted interests since they can be used to refine the solidification structure of the metal by promoting heterogeneous nucleation [23] or restraining grain size coarsening during the annealing process by impinging grain boundary migration [24]. By utilizing conventional casting processes it is difficult to evenly distribute these non metallic inclusions throughout the metal matrix still maintaining the high number density and narrow size distribution required to have the benefits listed above and little drawbacks [21]. By utilizing AM though, this is easier thanks to the quick solidification rate involved in these processes.

Oxygen content in components realized with DED is highly influenced by the process parameters chosen. Eo D.R. et al. have characterized non-metallic inclusions in AISI 316L stainless steel by studying distribution and their mean size and how these were varying when different process parameters were set, like a different laser power or a different scanning speed. The laser power highly influenced the oxygen content in the material, with an almost linear dependence. The scanning speed instead does not have an impact on the percentage of inclusions and their distribution, but only on their size. This is related to the fact that with an higher scanning speed the time the melt pool stays at a very high temperature is lower, thus leaving less time to the non-metallic inclusions to grow in size. Even with lower scanning speed

though, the inclusions that form during the DED process are very fine in dimensions, especially when compared with the ones obtained with conventional casting methods [21].

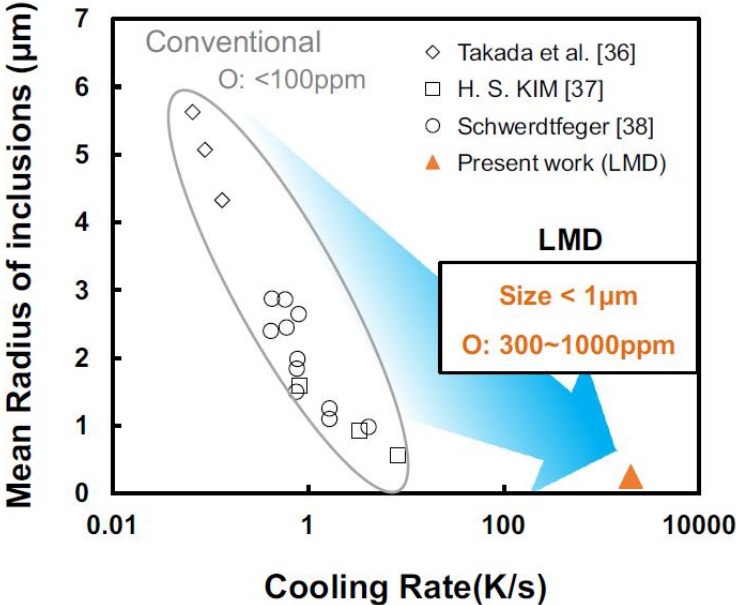


Figure 13 Non-metallic inclusions mean radius as a function of cooling rate for a conventional casting production process and a Laser Metal Deposition process [21]

2.7 Corrosion resistance

Corrosion is defined as a destructive attack of a metal by chemical or electrochemical reaction with its environment. Once these reactions start, a progressive deterioration of the properties of the material takes place as the product of the reactions are a different compound from the starting material [25]. It is of main importance to understand the phenomenon of corrosion because it has implications in many different aspects of society: economics, safety and conservation. Stainless steels are engineered to cope with corrosion better than other kind of steels and this characteristic has led to them being widely utilized. Their resistance to corrosion

comes from the passivating action the chromium dispersed in the steel has: when exposed to an oxidizing environment, a thin superficial layer of chromium oxides and hydro-oxides forms and this creates a shell that prevents further reactions that would involve the steel directly [26].

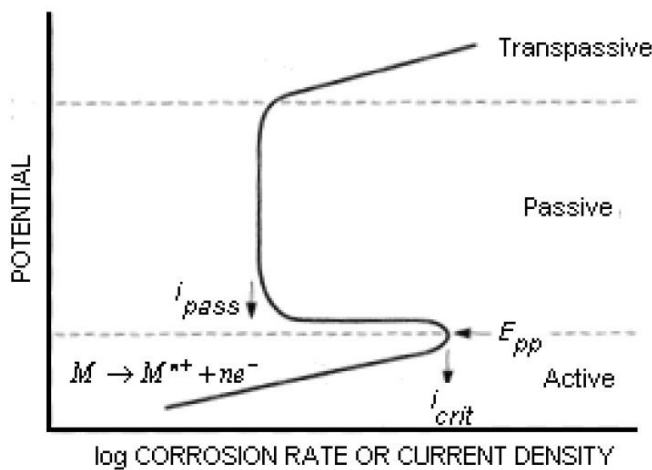


Figure 14 General stainless steel anodic polarization curve [26]

Figure (14) represents the polarization curve of a generic stainless steel. Different sections are clearly identifiable in the plot [26]:

- Active zone: the stainless steel behaves as a traditional steel, with the speed of the corrosion increasing as the potential increases;
- Passive zone: after the current reached its peak, the critical value (i_{crit}), in correspondence to the primary passivating potential (E_{pp}), it starts to decrease quickly thanks to the formation of the protective oxide layer. The current stabilizes at a very low and constant value i_{pass} and the speed of the corrosion is negligible thanks to the protection given by the surface passivating layer;

- Transpassive zone: as the potential increases the protective chromium oxide layer starts dissolving and localized corrosion takes place in correspondence of these spots where the passivating layer has been damaged.

Different types of corrosion exist, but the main ones can be divided into two categories depending on the amount of surface that is interested by the reaction: generalized corrosion happens when the whole surface is reacting, with cathodic and anodic areas being coincident, while localized corrosion happens when the cathodic zone and the anodic one are distant from each other. This latter kind of corrosion is more difficult to detect than the former one and can manifest itself in the form of pitting corrosion. When a component is affected by pitting its surface gets covered by small holes a few tenths of micrometres wide, as it can be seen in Figure (15). What can be seen from the surface of the component is just a very small part of the extent of the corrosion: under the external layer the cavity is much more pronounced and the mechanical and structural properties of the component can be compromised.

Pitting corrosion is particularly dangerous as it can happen in the steel passivation zone as well. The kinetics of this phenomenon can be divided in two phases: an initiation phase and a propagation phase. In the initiation phase the passivating layer of the steel is damaged by the corrosive action of some anions, especially Cl^- , in correspondence of some non-metallic inclusions or irregularities and the pit start to form. In the propagation phase, once the process has started, the pit expands as a current is generated between the areas where the oxide layer has been damaged and the passive zones that act as cathode. Two main reactions govern the propagation phase:

- An oxidation reaction of the metal at the anode, in the lower part of the pit, with the formation of metal cations;
- A reduction reaction of the oxygen in the cathode, the area right around the cavity.



Figure 15 Pitting corrosion on stainless steel [26]

Once the pit is formed it grows inside the metal, not on the component surface and this makes this kind of corrosion more difficult to detect. Moreover, the reaction is characterized by a very high kinetics and it is auto-catalysed: the products of the reaction contribute in making the environment even more aggressive for the metal [26].

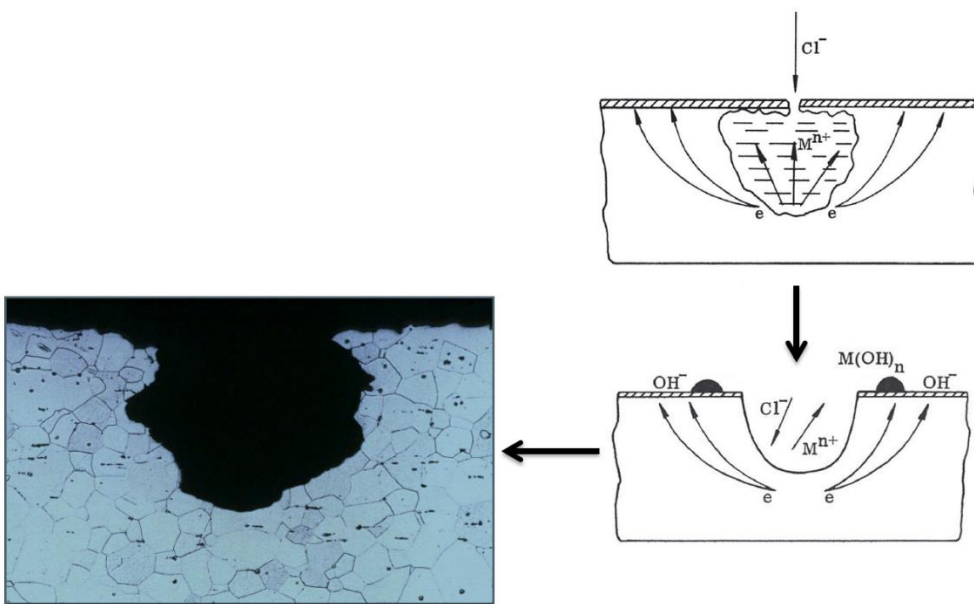


Figure 16 Pitting corrosion mechanism [26]

2.8 Materials

The materials of choice for this study are two different kinds of steels: AISI 304 for the sheet substrate and AISI 316L for the powder deposited. These are two austenitic stainless steels, highly corrosion resistant in a variety of different environments and especially at high temperature [33].

The AISI 316L is the low carbon version of the AISI 316 steel, with a carbon content equal to 0.03%. This reduces the chances for carbide precipitation and its possible interactions with chromium, that is thus free to form the passivating oxide film to protect the steel from corrosion. The chromium content is between 16.50% and 18.50%, while nickel is between 10% and 13%. The biggest difference between the AISI 304 and the AISI 316L is in the presence of 2.00% to 2.50% of molybdenum in the latter that gives the steel an even better corrosion resistance.

Element	% Present
Carbon (C)	0.03
Silicon (Si)	1.00
Manganese (Mn)	2.00
Phosphorous (P)	0.045
Sulfur (S)	0.015 ¹⁾
Chromium (Cr)	16.50 - 18.50
Nickel (Ni)	10.00 - 13.00
Nitrogen (N)	0.10
Molybdenum (Mo)	2.00 - 2.50
Iron (Fe)	Balance

Table 1 AISI 316L composition [34]

The microstructure of a steel component obtained by means of DED is different from the one of a conventionally produced piece. M. Zietala et al. [35] analysed in their paper the differences in microstructure and hardness of a 316L steel component produced using additive manufacturing. In their study, a steel cube is produced by DED and by means of a scanning electron microscope the material microstructure can be observed. The images reported in Figure (17) show a fine grain structure, with regions of elongated grains in the direction of heat dissipation. Moreover, mapping out the different steel phases, they found a higher concentration of face centred cubic phase than the original body centred cubic phase, in contrast with what can be found producing the component with traditional methods. The hardness of the component processed by DED was considerably higher than the one of the same components obtained by means of traditional manufacturing methodologies and subsequent thermal treatment: 289 ± 16 HV or 272 ± 35 HV (depending on the orientation, respectively perpendicular to the deposition direction or parallel to it) compared with 215-225 HV.

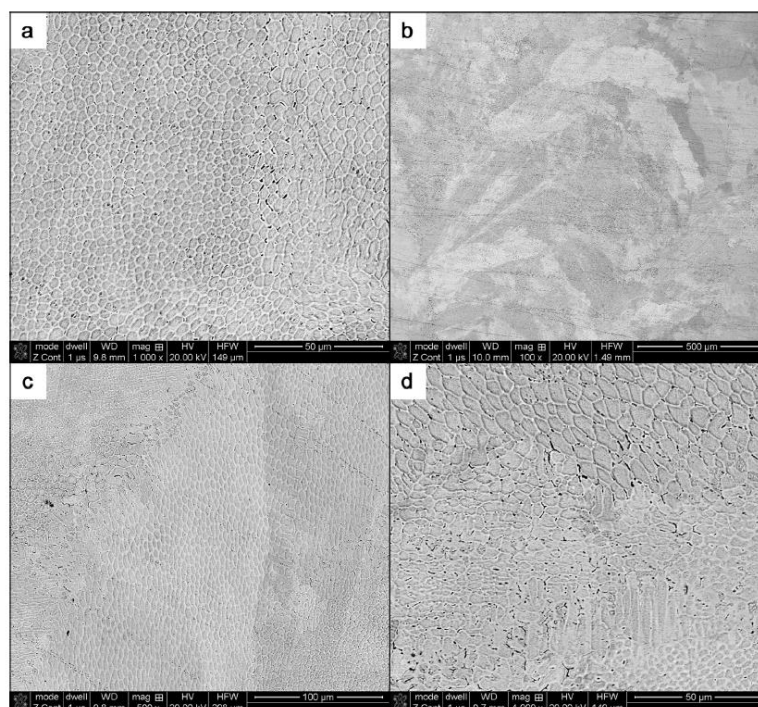


Figure 17 Microstructure of a 316L steel using DED: fine grain structure (a), islands of elongated grains (b and c) and finer grains (d) [35]

3. Experiment set-up

3.1 DED machine

The study proposed in this thesis has been carried out in the IAM Laboratory located in the Politecnico of Turin campus using a Prima Power Laserdyne 430 DED machine. This is a system with a three-axes control on the deposition plate and vertical movement on the deposition head. The maximum speed, being X/Y or Z direction, is 15 m/min. The deposition nozzle is a four-jet stream and argon is used as transport and shielding gas. The laser is up to 1000W. Additional information about the Laserdyne 430 are reported in the table (2).

Travel	X axis	585 mm (23.0 in)
	Y axis	408 mm (16.0 in)
	Z axis	508 mm (20.0 in)
	BeamDirector 3	900 degrees continuous motion in C axis 300 degrees continuous motion in D axis
Position speed	X and Y axes	15 m/min (600 in/min)
	Z axis	15 m/min (600 in/min)
	BeamDirector 3	0 - 90 rpm
Accuracy	X,Y,Z axes	12.5 μm (0.0005 inch) bi-directional
	BeamDirector 3	± 6 arcseconds
Resolution	BeamDirector 3	0.0005 degree
Repeatability	X,Y,Z axes	12.5 μm (0.0005 inch) bi-directional
	BeamDirector 3	within 6 arcseconds
Minimum programmable increment		2.5 μm (0.0001 inch)
Table Load Capacity		250 kg (550 lb)

Table 2 Laserdyne 430 specifications [35]



Figure 18 Optomec powder feeder

The powder is transported through the DED machine by argon and is stored in an Optomec powder feeder visible in Figure (18)

3.2 The study

There are different ways to reinforce a steel sheet using traditional methodologies and technologies, but the opportunity to use additive manufacturing for this purpose is enticing. For this study, the bending strength of a thin sheet of AISI 304 steel has been analysed and then compared with the results that can be obtained by depositing a thin layer of AISI 316L steel on top of it following different patterns. In order to do this the original steel sheet has been cut into multiple smaller pieces, measuring 25 mm by 50 mm. Some of these were kept as they were so as to have the blank sheet reference, the others were positioned in the DED machine to have different patterns of steel powder deposited on top. The choice of geometry for the deposited steel powder was identified into three main types: longitudinal relative to the sample, transversal and at a 45° angle. For each of these geometries there will be two different kinds of deposition: one with separated deposited lines and one with merged ones. The total width of the deposition area is constant for every sample, at 10.5 mm.

Regarding the deposition patterns, different strategies were available, as illustrated in chapter 2.2, and considering the simple shape we had to deposit as well as the fact that is a single layer deposition, we decided to go for the zig zag pattern as it was able to spread the heat effectively reducing the amount of warping of the steel sheet. Some seconds of cool down were waited before the deposition head inverted its movement.

3.3 Preliminary test

As explained above in chapter 2.1, the parameters to be tuned in order to get the best results possible with a directed energy deposition machine are plentiful. To determine the right parameters for the application in this study some tests were performed, considering mainly three key parameters: the laser power, the deposition speed and the powder flow rate.

Considering previous experiences with the same DED machine, the range of values of the three main process parameters identified are:

- Power: 400 W, 550 W, 700 W;
- Deposition speed: 600 mm/min, 700 mm/min, 800 mm/min;
- Powder flow rate: 7 rpm, 8rpm, 9 rpm. (The powder flow rate is proportional to the rotational speed of the feeder).

A trial-and-error approach using these three factors with three levels each would have required a total of 27 tests. This was deemed too labour extensive and a waste of resources and time, so Taguchi approach was used and only 9 tests were performed. The different combinations of the process parameters for each trial are reported in Table (3).

Test number	Laser Power [W]	Deposition Speed [mm/min]	Powder flow rate [rpm]
1	400	600	7
2	400	700	8
3	400	800	9
4	550	600	8
5	550	700	9
6	550	800	7
7	700	600	9
8	700	700	7
9	700	800	8

Table 3 Different combinations of the three main parameters for the deposition tests

All the tests were performed on the same steel sheet and the results are visible in Figure (19). The quality of the deposition varies wildly between the different tracks, but it wasn't difficult to identify the best ones. Tracks 1 through 3 all have a clear lack of powder merging: the laser power wasn't enough to melt the powder, not even for the slowest deposition speed test, and the resulting tracks are not acceptable. Increasing the laser power to 550 W, tracks 4 through 6, resulted in more even deposited tracks. In particular, looking at test number 5, can be seen that there is a lot of powder not melted in the track, but solidified around it: this is an indication of the powder feeder rotational speed being too high for the other process parameters chosen. Tests number 4 and 6 both have a more defined deposited track with fewer side powder stuck on. Looking at the track itself, the width of test number 4 is larger. This makes sense because it has a larger amount of powder being blown through the deposition nozzle and, at the same time, a slower deposition speed, giving the laser more time to heat up the melt pool. The best results though were obtained with the highest

laser power parameter. Tracks 7 through 9 were all more defined, with smaller and fewer side powder and a wider deposited track. Among these tests, test number 7 looks like the worst one: the highest powder feeding rate resulted in a lot of tiny powder particles not been properly melted into the main track but being scattered all around the deposition track. Between test number 8 and test number 9 there wasn't too much difference in terms of quality of the track, but the slower deposition speed of test number 8 meant a larger amount of heat was transferred by the laser to the steel substrate and this led to a more pronounced deformation of the alloy sheet. This is why higher laser powers were not investigated even if the laboratory equipment could handle them. The process parameters chosen for the study proposed in this thesis were thus the ones of test number 9, resulting in a width of the deposited line of 1.5 mm.

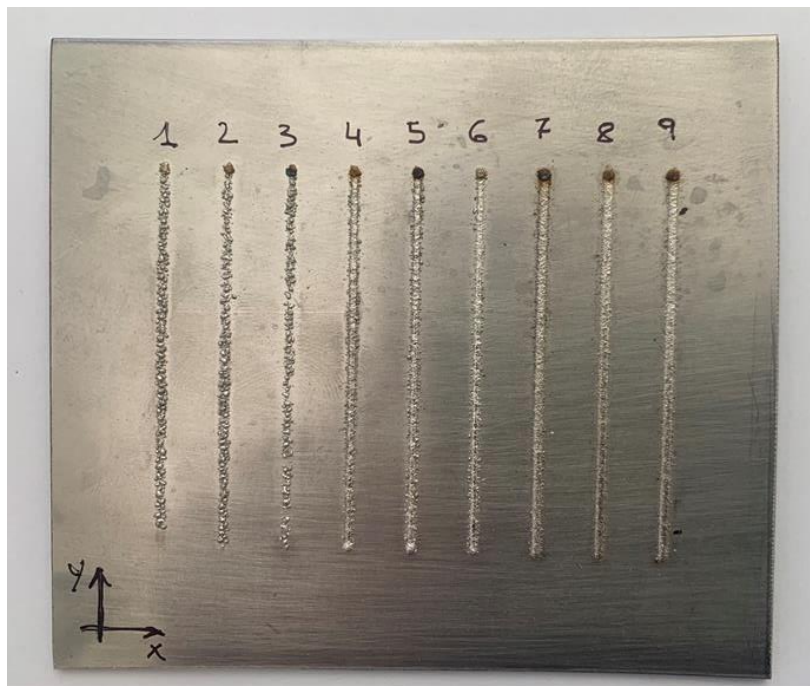


Figure 19 Deposition tests to determine the best DED parameters pre-sets.

3.4 Bend Test machine

The bending test is performed by a hydraulic 3-point bending machine. The test piece is positioned on top of the two extreme steel cylinders while the central one is slowly lowered to deform the specimen. The two supports are movable in order to allow the testing of larger specimens and the distance between them has been computed according to the standard ISO 7438:2020. The formula to compute such distance is:

$$l = (D + 3a) \pm \frac{a}{2} [36]$$

where D is the diameter of the supports (that has to be equal to the diameter of the former as well), a is the thickness of the test piece and l is the distance between the supports.

The speed of the former was set to 2 mm/min and the end of the test was set at a travel distance of the former equal to 9 mm. A longer travel was not possible as the test piece would have contacted the machine structure invalidating the results. To ensure repeatability and a correct positioning all the samples were loaded into the machine using a metal bracket as a reference, visible in Figure (20). During the test the load exerted by the former was logged as a function of the distance travelled so that a comparison with the different specimen was possible. All the test pieces survived this test without any visible surface cracks.

With the maximum load endured by the test piece it is then possible to compute the maximum fibre stress as:

$$S = \frac{3PL}{2bd^2} \quad (1)$$

where P is the maximum load, L is the span of the two supports, b is the width of the specimen and d is its thickness [37].

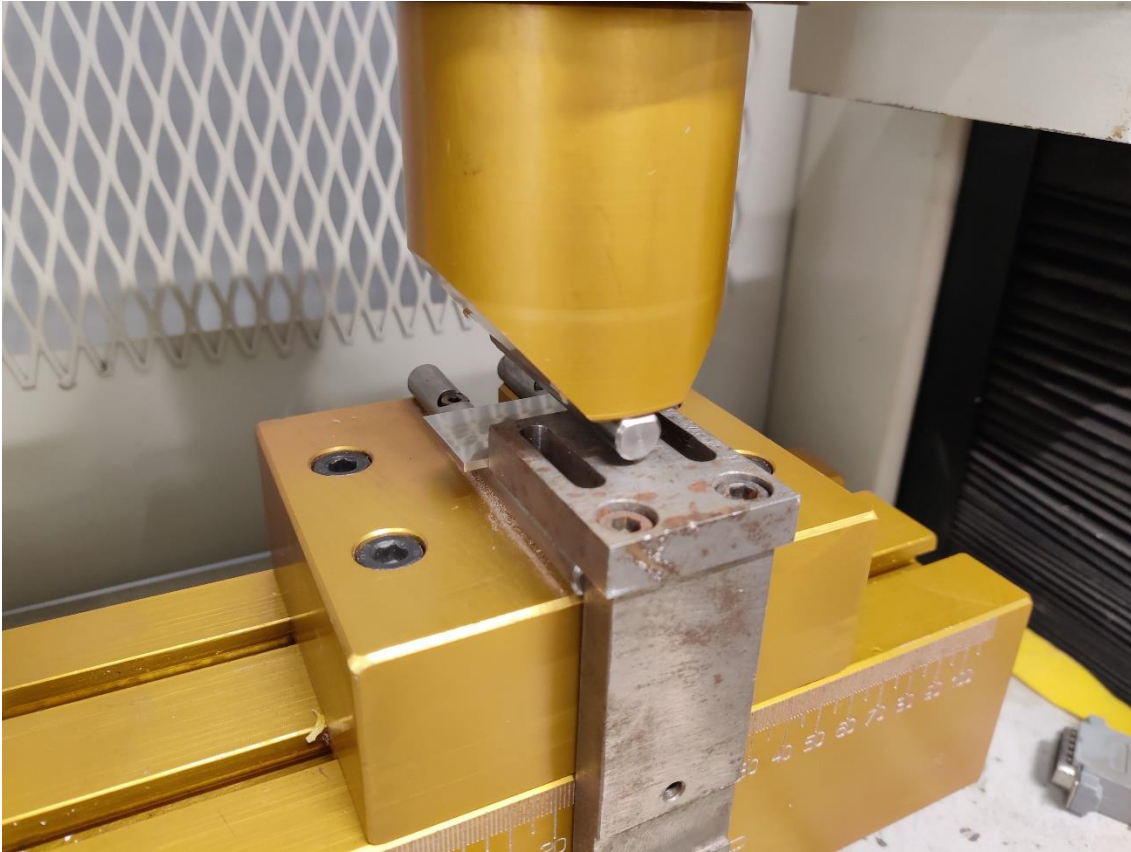


Figure 20 Detailed shot of the bend test machine. The metal bracket used to align the test piece is clearly visible.

The standard ISO 7438:2020 also specifies the procedure to compute the bend angle α measuring the displacement of the central loading point:

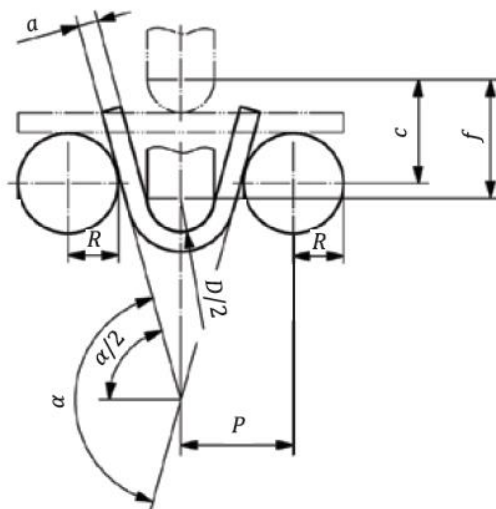


Figure 21 Bend angle test drawing [36]

$$\sin \frac{\alpha}{2} = \frac{p \times c + W \times (f - c)}{p^2 + (f - c)^2} \quad (2)$$

$$\cos \frac{\alpha}{2} = \frac{W \times p - c \times (f - c)}{p^2 + (f - c)^2} \quad (3)$$

$$W = \sqrt{p^2 + (f - c)^2 - c^2} \quad (4)$$

$$c = R + a + \frac{D}{2} \quad (5)$$

where p is the distance between the vertical planes including the central axis of each support and the vertical plane including the central axis of the former, c is the distance between the plane including the horizontal axis of supports and the central axis of the rounded portion of the former before test, f is the displacement of the former, R is the radius of the supports, a is the thickness of the test piece and D is the diameter of the former. All units are considered in mm.

Former travel [mm]	Bend angle α [°]
0	0.0
1	9.1
2	18.9
3	29.4
4	40.4
5	52.1
6	64.3
7	76.9
8	89.6
9	102.2

Table 4 Bend angle as a function of the distance travelled by the former, according to equations (1) through (4)

3.5 Microscope



Figure 22 Leica S9i microscope. Under the light is the deposition test steel sheet

The microscope of choice is a Leica S9i stereo microscope, with a magnification of up to 55x [38], plenty enough to resolve every powder particle in the deposition tracks on the samples. The integrated camera made the analysis of the sample easy and the software connected to the microscope allowed for the measurement of the details we were interested in.

3.6 Experiment setup

To prepare the different samples to be tested the original AISI 304 steel sheet had to be cut down into multiple smaller pieces, all measuring 80 mm by 100 mm. These are bigger than the final samples and this allows us to place them more easily into the DED machine, as well as cutting out the extremes of the deposited tracks, keeping only the steady state central portion. Once these components were obtained, the surface was cleaned and hand sanded in order to reduce the reflectivity of the metal prior to the deposition into the DED machine. This was not a strictly necessary step, but it was not time consuming and ensured even surface conditions for every sample, moreover a less reflective surface is more suitable to laser additive manufacturing procedures.

To proceed with the deposition, the G-code for the DED machine had to be written. In order to do this the desired geometry and the strategy of the deposition had to be clear. As anticipated in chapter 3.2, the comparison analysed in this study is among three different deposition geometries and two different versions for each of those, merged deposition tracks and separated deposition tracks. Below are shown the different samples. The 25 x 50 mm dashed rectangle is the final test piece that will be cut and bended.

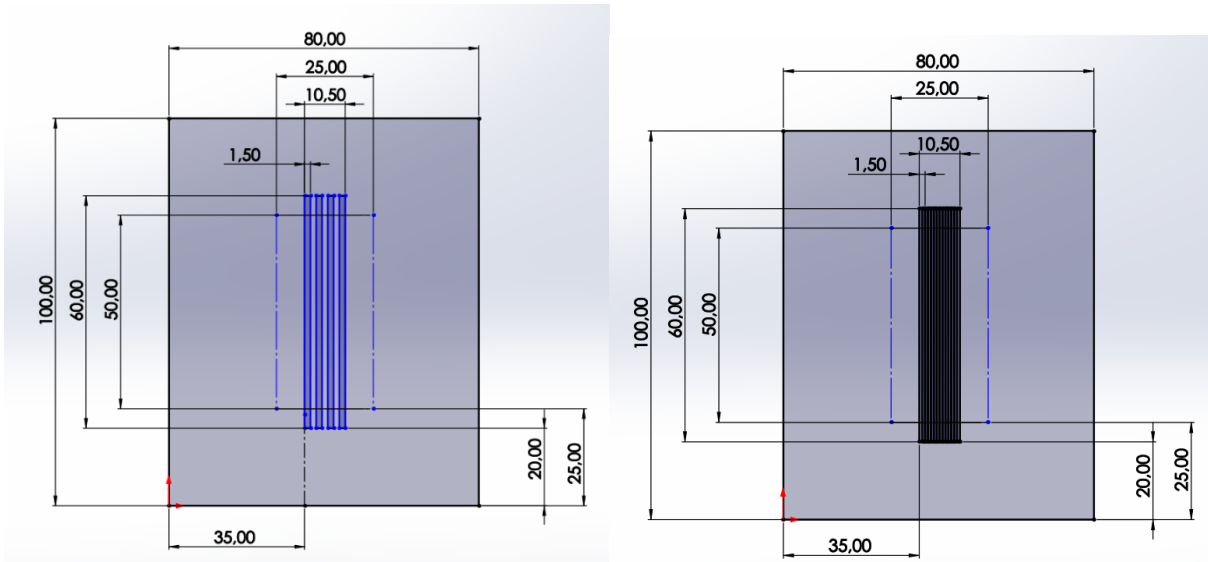


Figure 23 Vertical separated (left) and merged (right) deposition tracks test pieces.

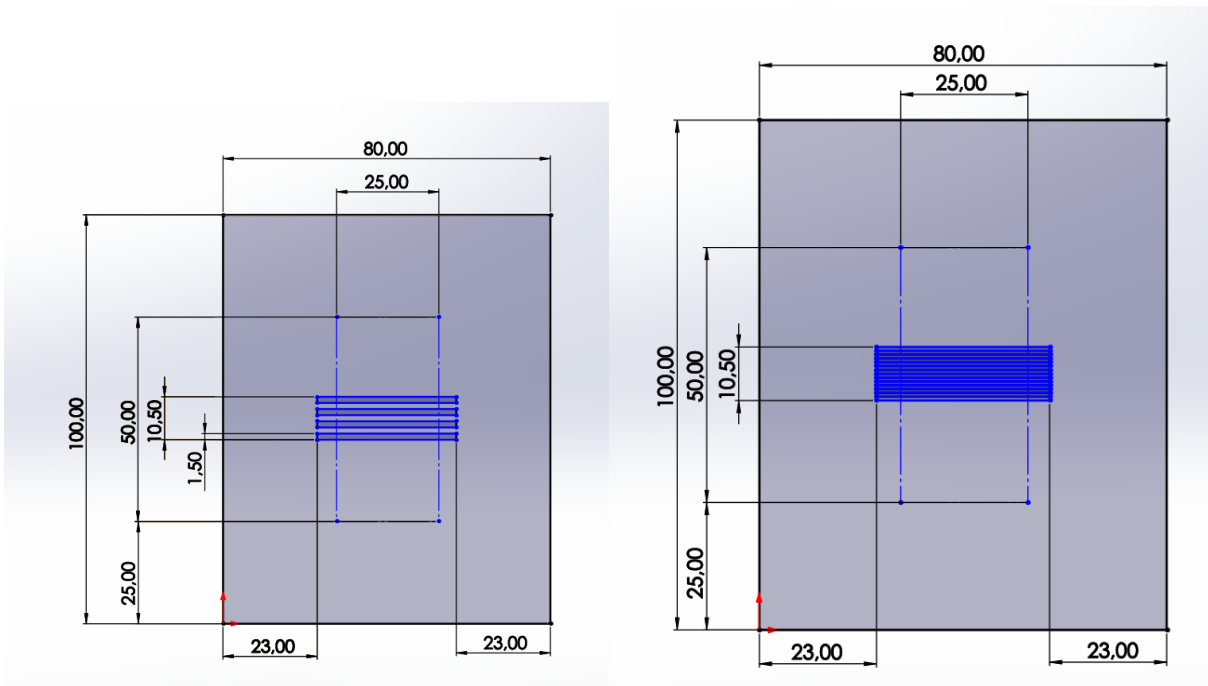


Figure 24 Horizontal separated (left) and merged (right) deposition tracks test pieces.

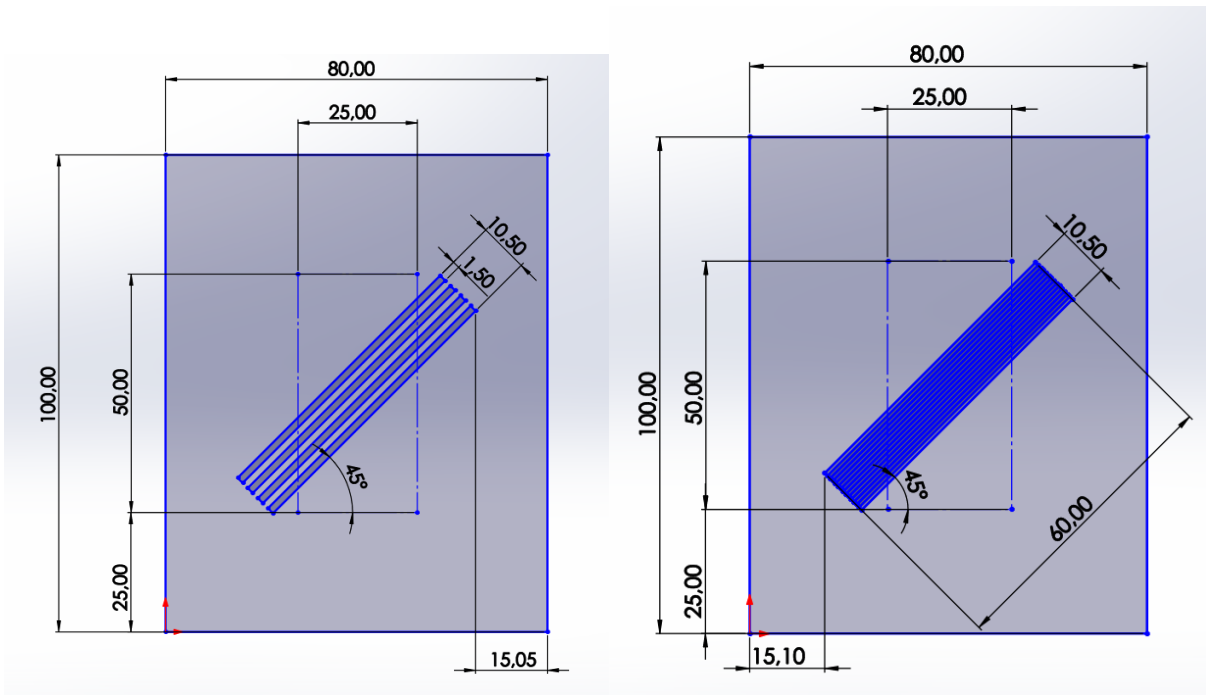


Figure 25 Diagonal separated (left) and merged (right) deposition tracks test pieces

Once the correct G-code was uploaded on the DED machine it was time to fix the first substrate. We needed a fast and reliable method given the quite high number of samples to be produced, so we opted for four tightening, one for every side of the steel sheet (Figure (29)). Once in place we had to set the zero of the coordinates on the machine's software. Thanks to the camera built into the deposition head this wasn't difficult to accomplish and this was a good thing as the alignment of the steel substrate wasn't exactly the same for every sample: at this point the AISI304 steel sheet was cut without too much attention on dimensions as the real samples would be cut after the depositions. With everything in place, it was time to simulate the deposition, to make sure that nothing was on the way of the deposition head. Once this step was cleared, we started with the first depositions, proceeding first with the five samples with vertical separated tracks, then the five with vertical merged tracks and so on. At the end we got our 30 deposited sheets ready to be cut to size in a horizontal saw. The edges of the samples were then refined on a sander. Once cleaned,

the samples were then analysed under the microscope, tested in the bending machine and then observed under the microscope again.



Figure 26 A test piece inside the DED machine after the deposition

4 Analysis

4.1 Photo analysis

The samples produced turned out well and the simplicity of the deposited geometry didn't cause any problem whatsoever with the DED machine. In Figure (30) are shown all the different pieces that will be analysed. The deposited tracks are clean and regular, and the amount of excessive steel powder is not overwhelming and in line with the test made prior to the experiment (see chapter 3.3). The distortion of the steel sheet due to the heat it was subjected to during the deposition procedure was limited and wasn't concerning, but higher laser powers would have resulted in quite deformed steel substrates for sure.

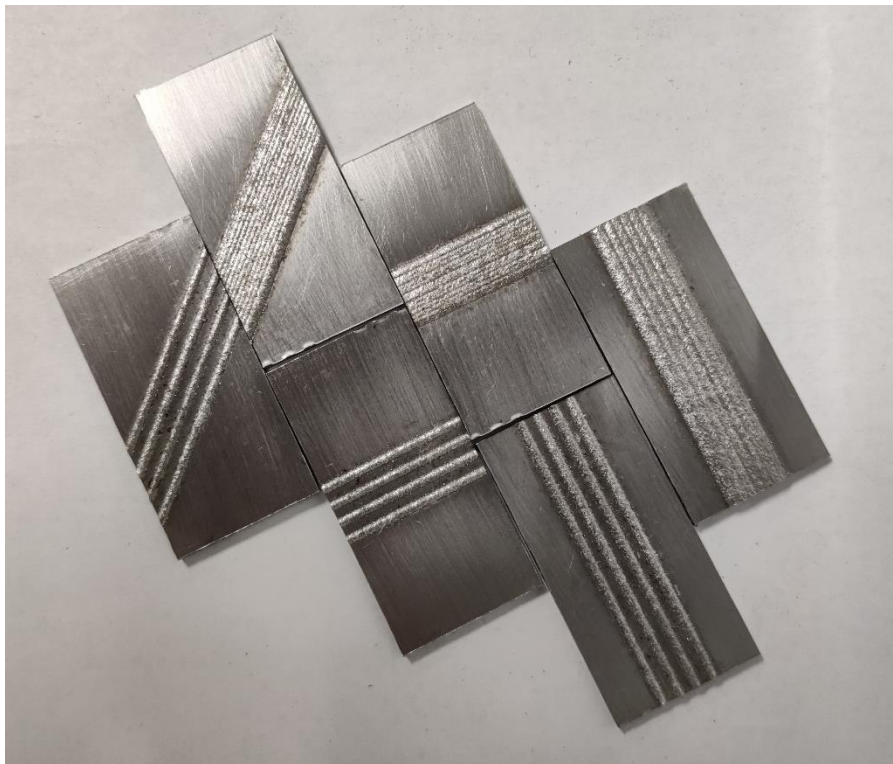


Figure 27 All the different test pieces geometries

4.1.1 Vertical Depositions

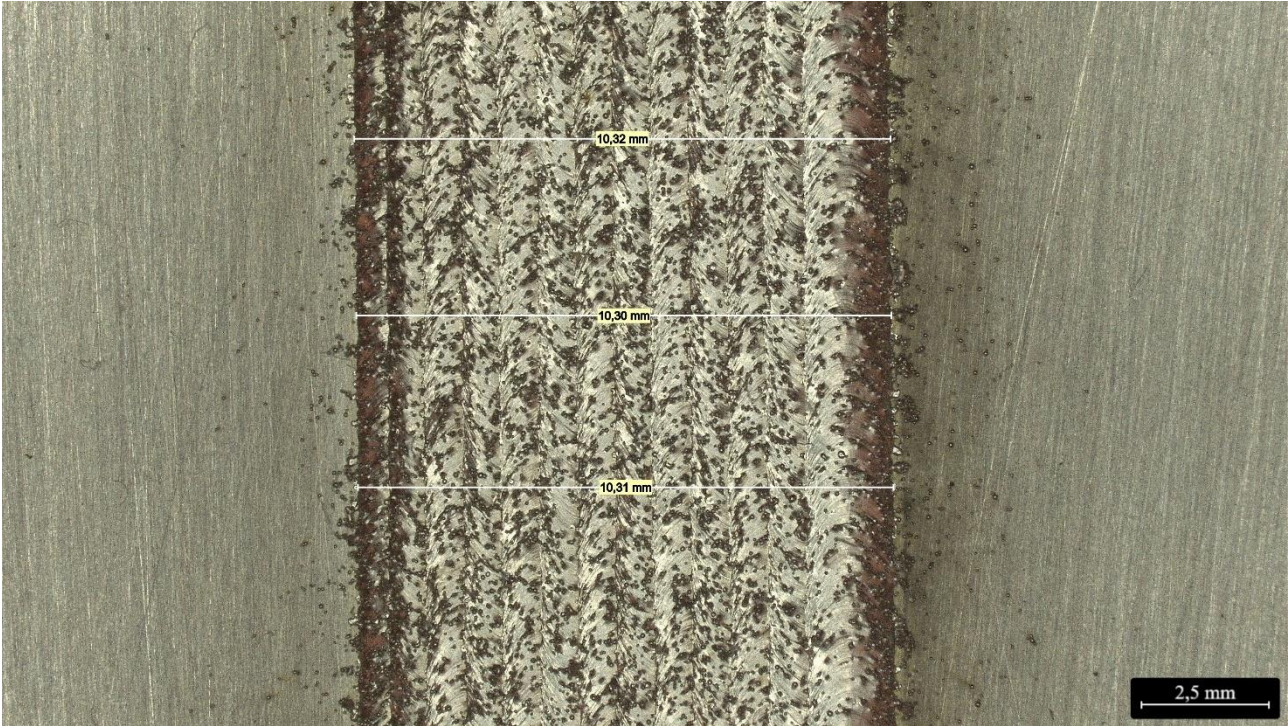


Figure 28 Vertical merged deposition microscope close-up

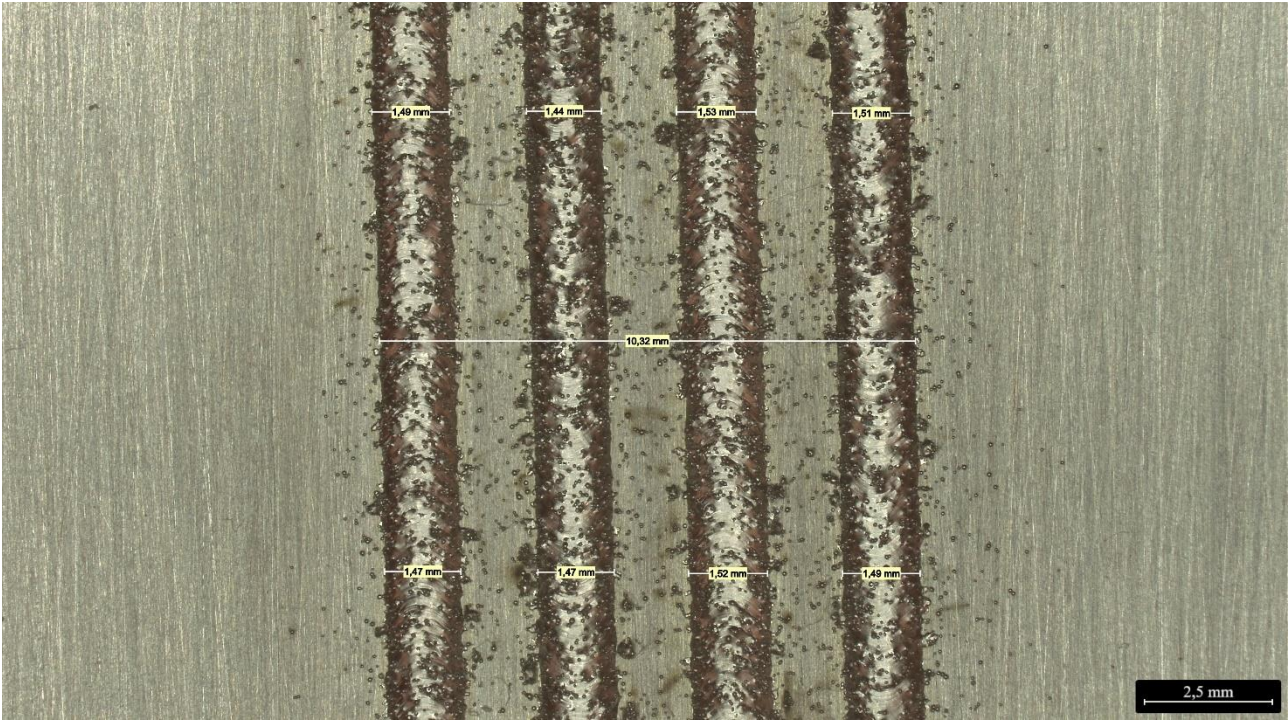


Figure 29 Vertical separated deposition microscope close-up

The depositions look regular and well defined, with little excess powder. By using the microscope software, I was able to measure the distance of different points in the two samples. The repeatability of the tracks' width is quite good, and the different values indicated in the pictures above prove that. Anyway, at this level of magnification it was quite difficult to keep a consistent reference point for the determination of the measurement as the small irregularities in the shape of the track easily produced outlier values. The theoretical deposition track's width was 1.5 mm, and for both the merged and the separated tracks the total width of the deposition should have been 10.5 mm. In reality, for both samples, we got something less than that: a reduction of about 2%. If that's too high or not was not an issue for this thesis study as this reduction in deposited width was consistent among all the samples tested.

4.1.2 Horizontal Depositions



Figure 30 Horizontal merged deposition microscope close-up

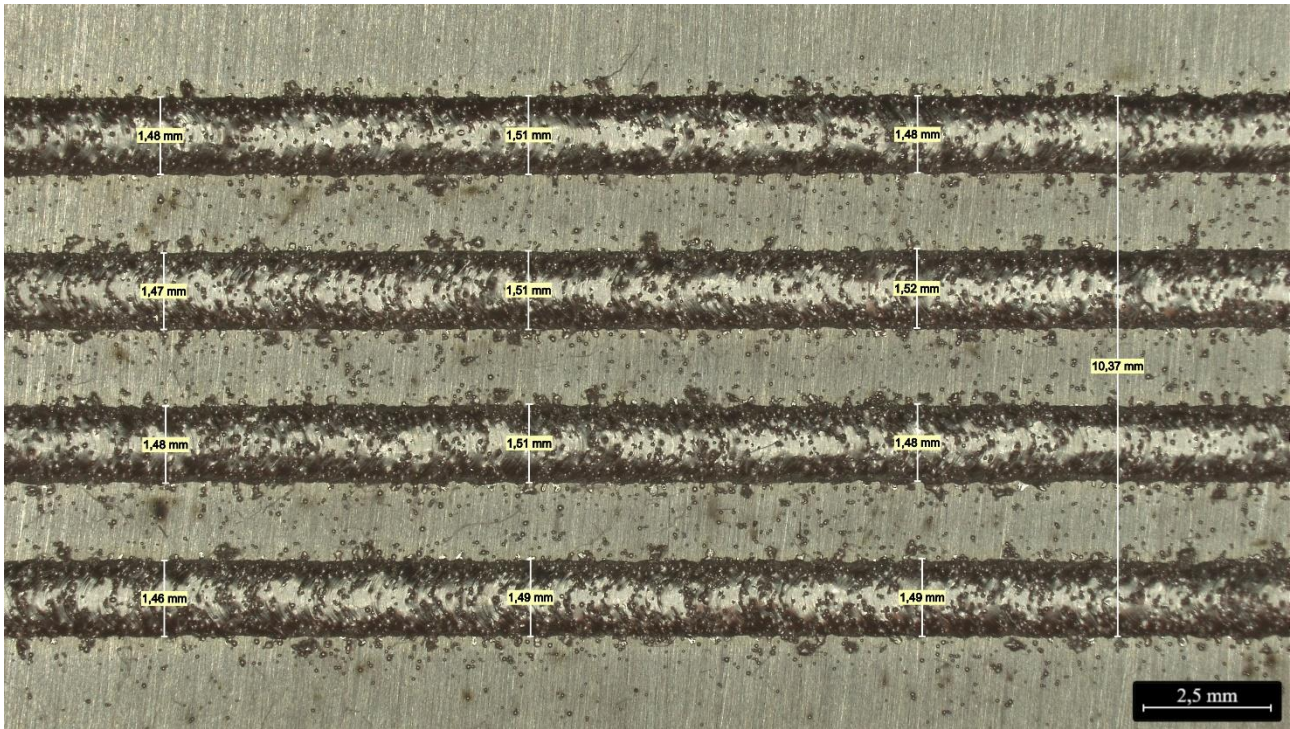


Figure 31 Vertical separated deposition microscope close-up

The depositions look good and quite regular for this category of samples as well, just like the vertically produced pieces did. After all, DED machine conditions were kept the same and was only the pivotal base of the printing enclosure that was rotated by 90°. Looking at the measurements, we can see the same level of variability again, but an overall width a bit higher. This is probably due to the measured spot only, given that, as stated earlier, the little irregularities were big enough to change what are effectively microns differences in the total width, just a few percentage points relative.

4.1.3 Diagonal Deposition



Figure 32 Diagonal merged deposition microscope close-up

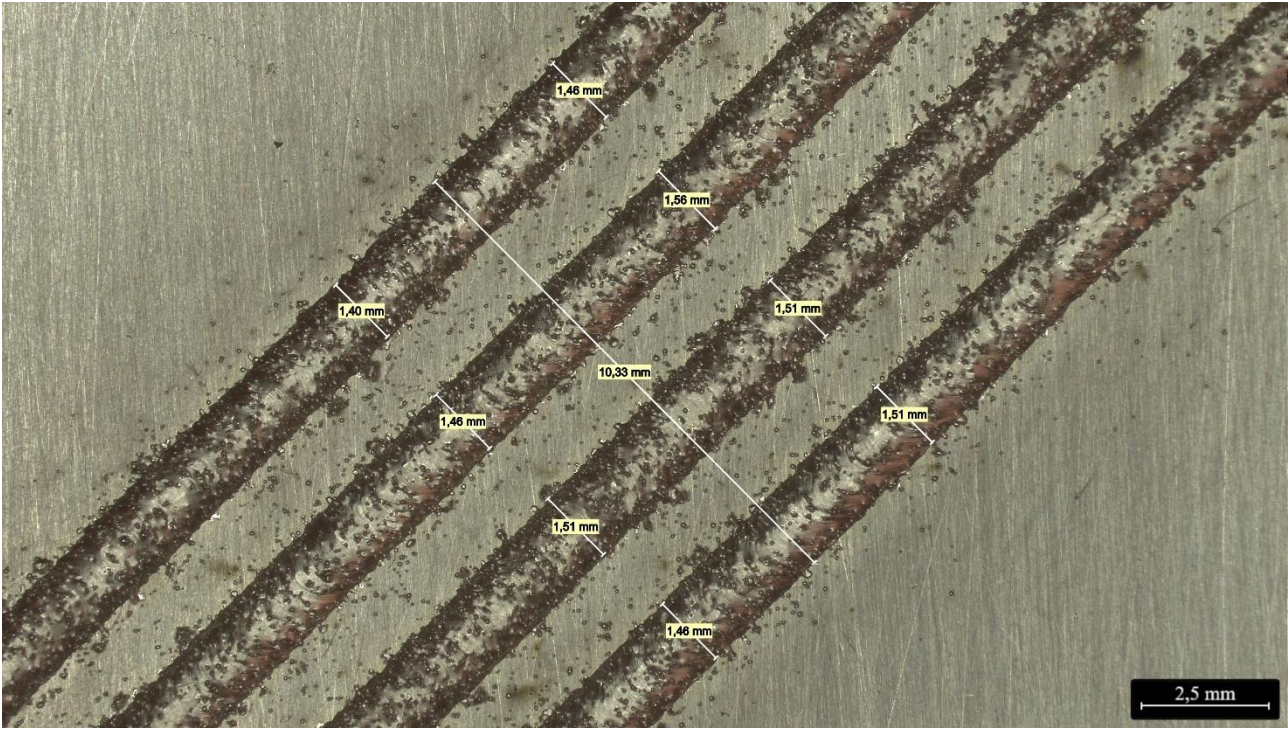


Figure 33 Vertical separated deposition microscope close-up

This diagonal deposition doesn't look dissimilar from the previous two different kinds of samples: the deposited tracks are nice and clean and quite regular in size. Again, the only difference in the DED machine parameters was the rotation of the printing enclosure base.

4.2 Bend test

Once the samples were analysed under the microscope it was time to perform the bend test as described in chapter 3.3.

The output of the bending test machine is a text file with the logging of the different values of force applied to the test piece by the central former as a function of its displacement. A Matlab code has been written in order to analyse the text file and plot the data for a better understanding of the single bend test and for comparison among the different kinds of samples.

A question that arose before performing the tests was whether to perform the bend test with the deposited tracks on the tension side of the specimen or on the compression side. To answer this, and to see if there were any significant differences between the two case studies, four samples, with vertical separated deposited tracks, were tested: two of them were positioned with the added material on the tension side and two on the compression side.

The very first test performed was with the tracks on the compression side and it was executed a day in advance compared with the others. At the time we positioned the specimen in the machine without any guidance and we performed the test. At first glance everything looked fine, but once we repeated the same test with the other samples the following day using the metal bracket for a

correct positioning, we realized that the first specimen must have been incorrectly positioned as the results of that test were way off the others, with much lower values of force needed to perform the test. For this reason, the very first test was excluded from the analysis, leaving one sample tested with the deposition on the compression side and two on the tension side. The results are plotted in Figure (37).

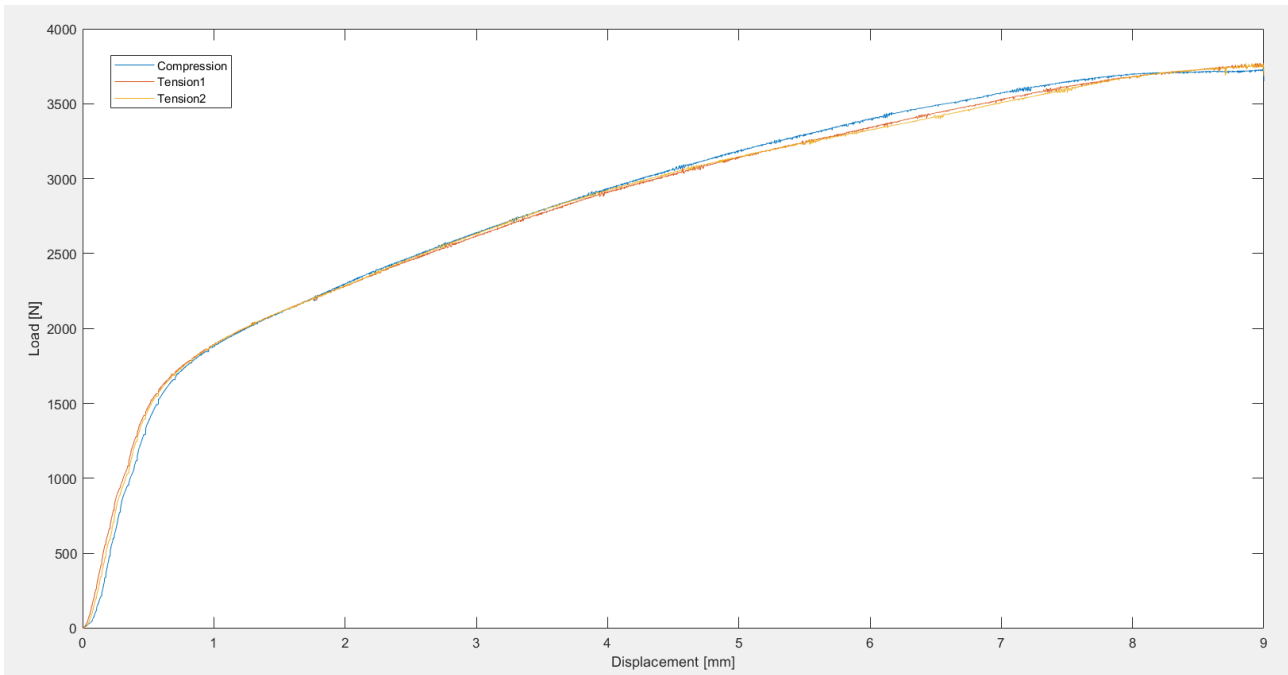


Figure 34 Comparison between the same geometry placed in the bend test machine with the depositions on the compression side or on the tension side.

To better understand what on the global scale of the experiment look like very similar curves let's look at some close ups.

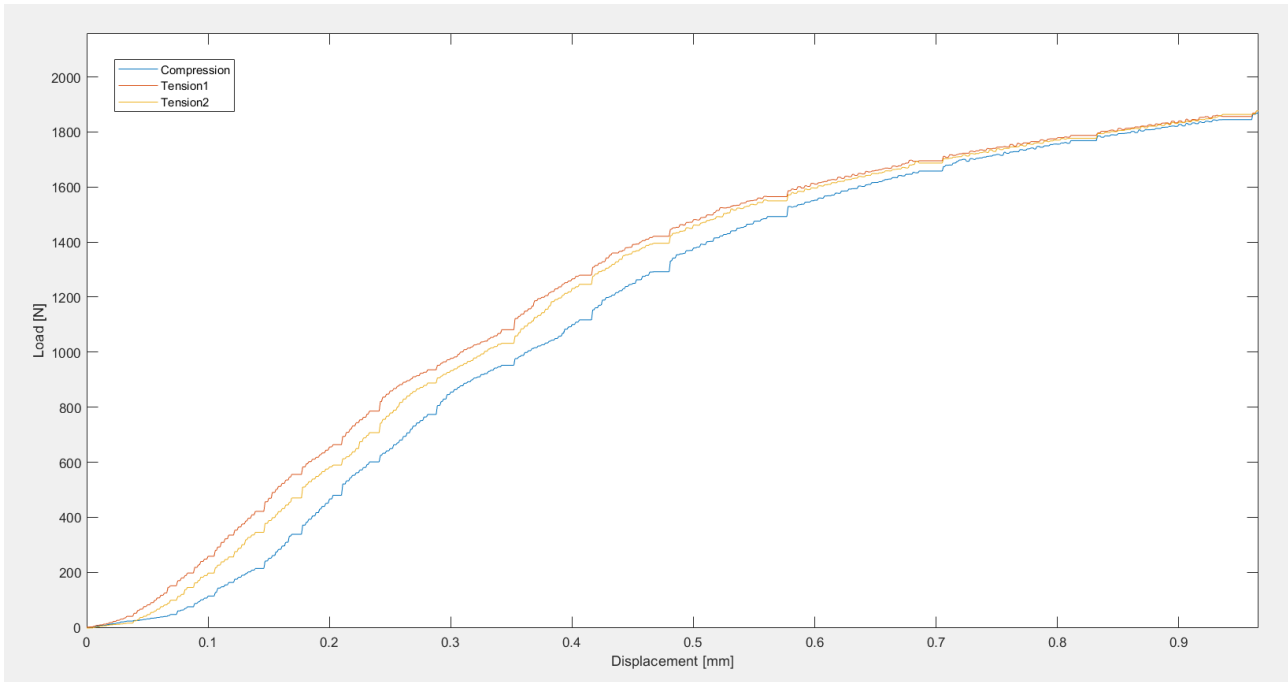


Figure 35 First millimetre of travel of the former, plot extrapolated from Figure (37).

In the first millimetre of travel, the two specimens with the deposition on the tension side are always above the line of the one with the deposition on the compression side. This is particularly evident in the first half of this magnification: for example, at a displacement common among the three samples of 0.2 mm, the compression specimen registered a force of 451 N, while the two in tension respectively 575 N and 644 N. At this small displacement the differences are notable, with an increase in the force needed for the bending of 27.5% and 47.8% by only changing the orientation of the sample. At 0.5 mm the three samples were closer together, but the disparity among them still stood as before: the sample with the deposition in compression registered 1370 N, the ones in tension 1450 N and 1472 N, that is an increase of 5.8% and 7.4% respectively. Once the bending machine central former reaches 1 mm of travel the three specimens are basically equal in the amount of force needed, at 1880 N. Keep in mind that this displacement corresponds to a bending angle equal to 9.1° (according to equations (2) through (5) in chapter 3.3). The behaviour

keeps staying the same up to more or less 4 mm of travel, where the different lines diverge a bit again.

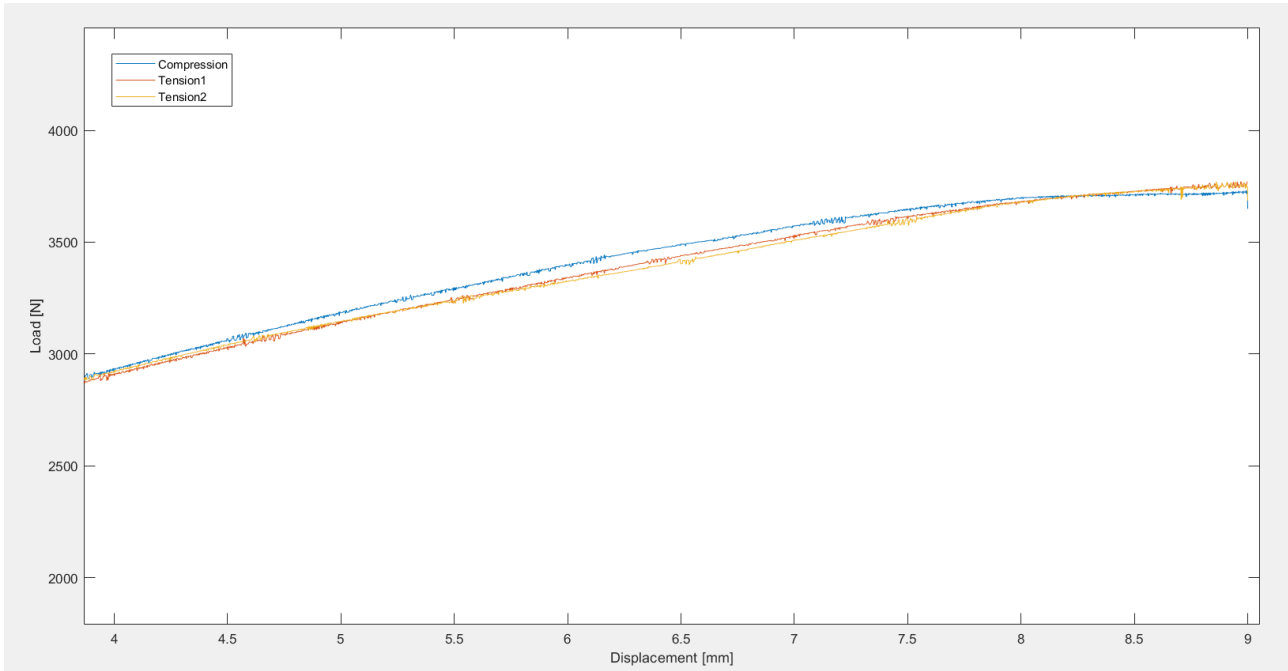


Figure 36 38 Second half of travel of the former, plot extrapolated from Figure (37).

Here the specimen with the depositions on the compression side is the one that registers the highest force among the three. At a displacement of the former of 6 mm the force required is 3396 N for the specimen with the deposition on the compression side and 3325 N and 3342 N for the two with the depositions on the tension side, but the difference is smaller, being a reduction in the force needed of 2.1% and 1.6% going from the compression side arrangement to the tension side one.

Finally, at a displacement of more or less 8.2 mm, the behaviour switches again and the two samples with the deposition on the tension side keep building up the force required for the bending, while the specimen with the deposition on the compression side plateaus. The maximum force required by the sample in compression was 3731 N while for the two in tension 3769 N and 3771 N.

Overall, the difference wasn't much between the two arrangements, but considering especially the behaviour in the first stages of the test it was decided to place all the specimens with the deposited stripes on the tension side during the bending test. Every sample was tested in the same conditions and tests were performed one after the other for each kind of deposition pattern: first all the five vertical depositions with separated tracks, then the ones with merged tracks, then the horizontal ones and so on.

4.2.1 Blank sheet bend test

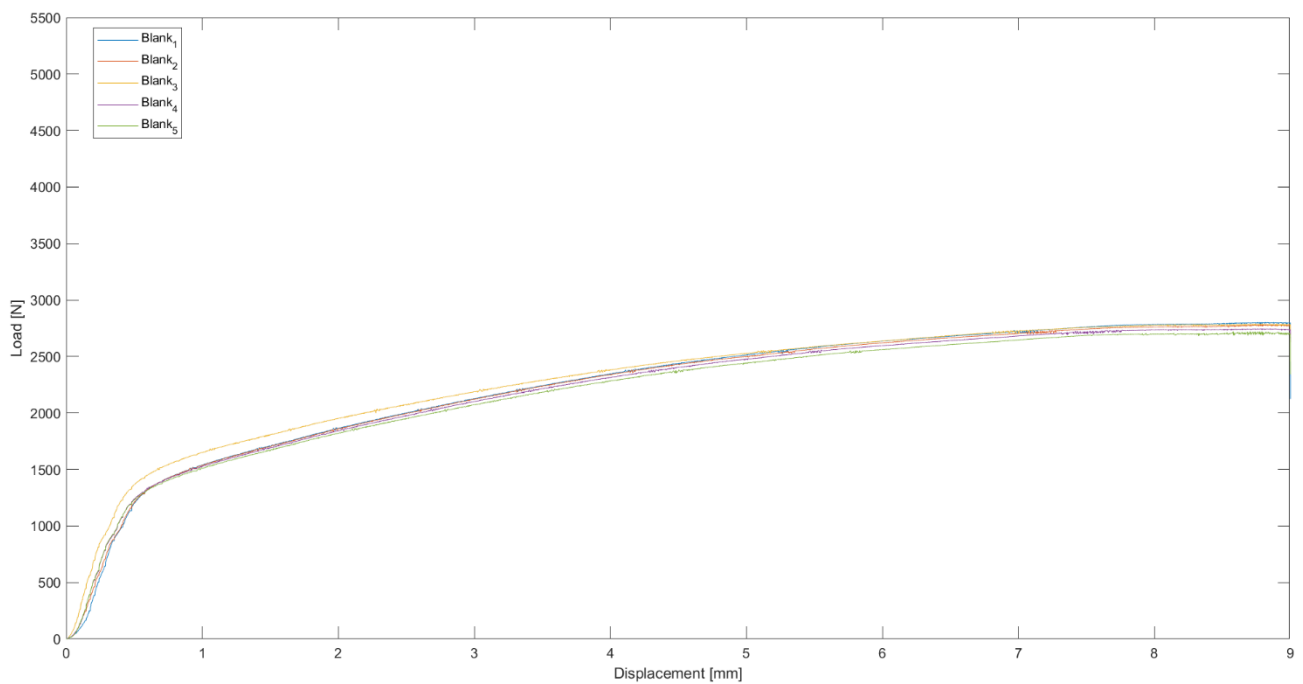


Figure 37 Comparison of the results of the five blanks bend test

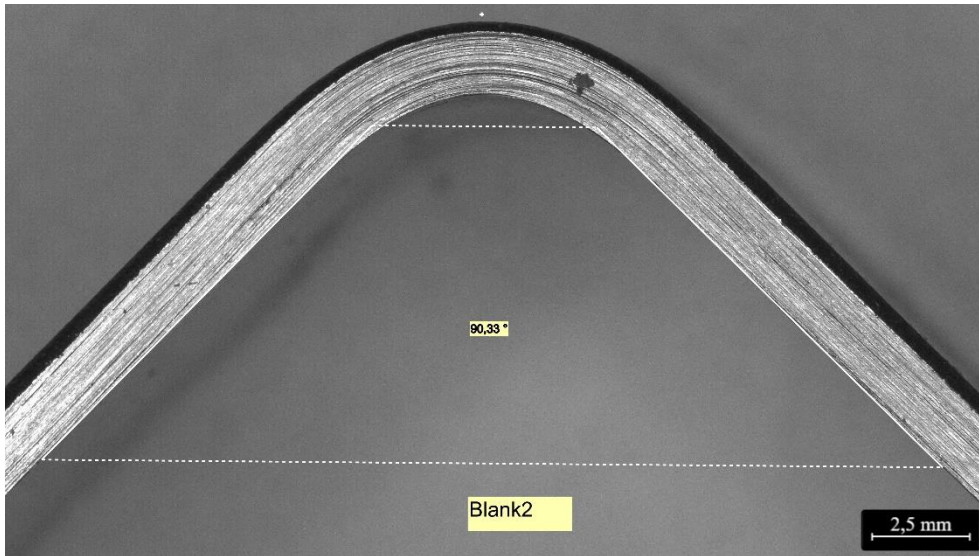


Figure 38 Blank test piece after the bend test. Picture taken with the microscope.

The trend of the load exerted by the central former is plotted as a function of its displacement is plotted in Figure 40 for the blank steel sheet, without any deposition to stiffen it. As the load is applied, the specimen bends and for the initial part of the test the load increases with a quite high rate. Once the displacement is around 0.5/0.6 mm a variation in the rate of change of the load can be appreciated: the slope of the curve flattens as the specimen continues bending more and more. At 0.6 mm of displacement the highest load is endured by specimen number 3, at 1460 N, while the other four are basically equal, at 1405 N.

The maximum loads reached during the test were quite similar to one another, with the highest being by sample number 5, at 2804 N, and the lowest by sample number 2, at 2557 N. Maximum fibre stress ranged from 997 MPa of sample number 2 to 1094 MPa of sample number 5. All the results are reported in table 5.

Keeping in mind that to a displacement of the central former of 9 mm should correspond a bending angle of 102.2° (equations (1) through (4)), the result measured under the microscope represents a quite high elastic return: the test specimen had a bend angle of 90.33° .

Specimen	Maximum load	Maximum fibre stress
/	N	MPa
Blank1	2647	1043
Blank2	2557	997
Blank3	2794	1090
Blank4	2789	1088
Blank5	2804	1094

Mean value	σ	Mean value	σ
2723 N	107 N	1062 MPa	42 MPa

Table 5 Bend test results for the blank test pieces.

4.2.3 Vertical depositions bend test

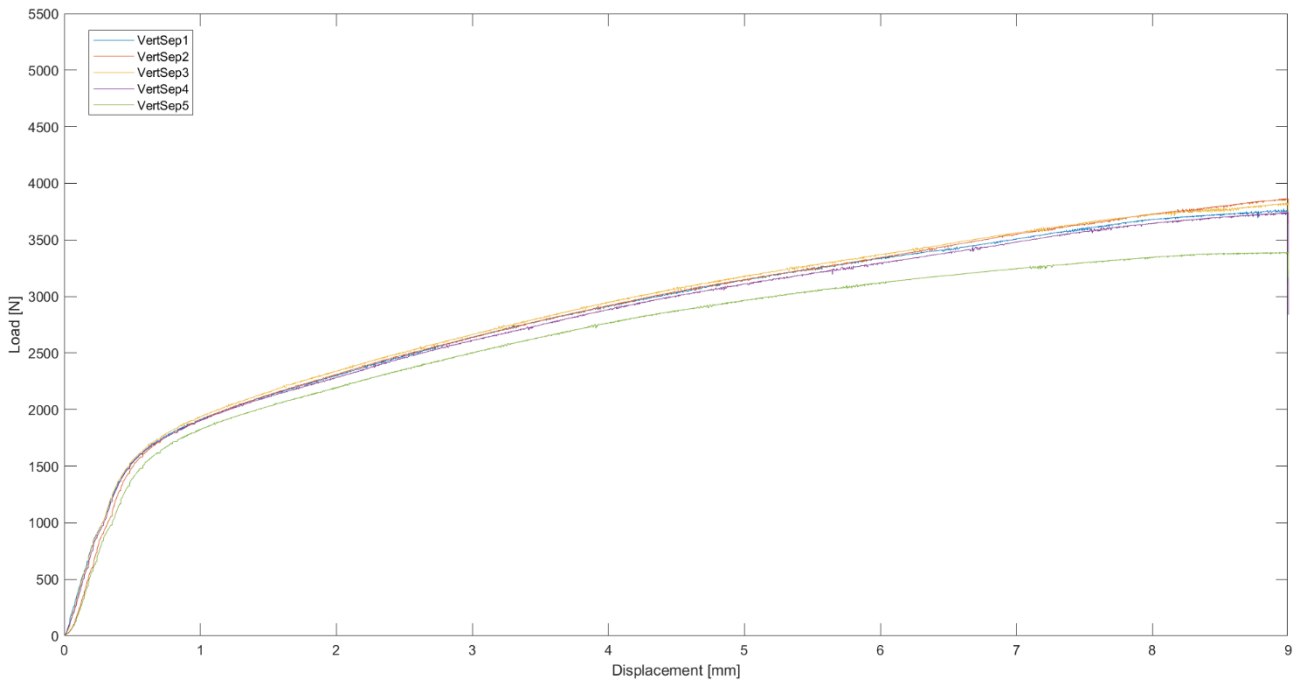


Figure 39 Comparison of the results of the five vertical separated depositions bend test.

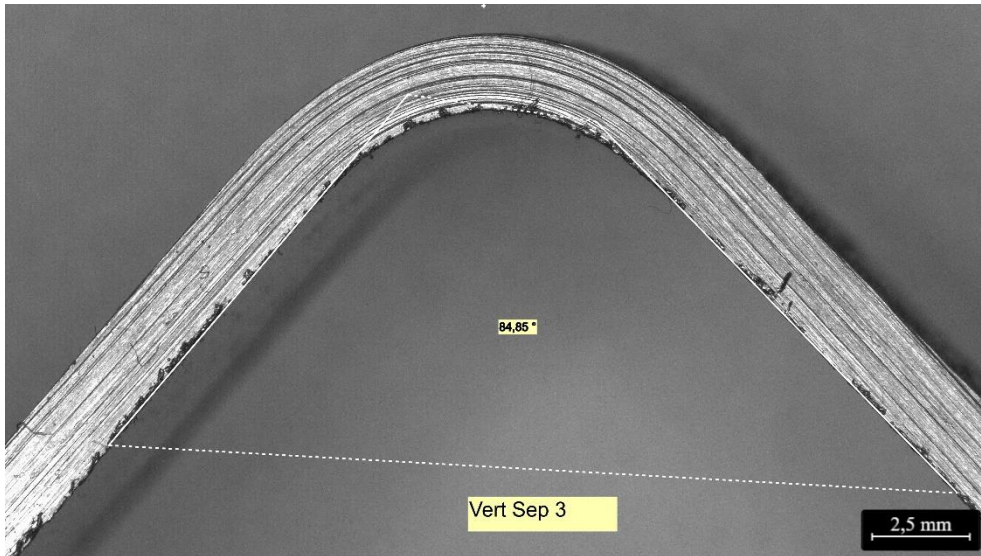


Figure 40 Vertical separated deposition test piece after the bend test. Picture taken with the microscope.

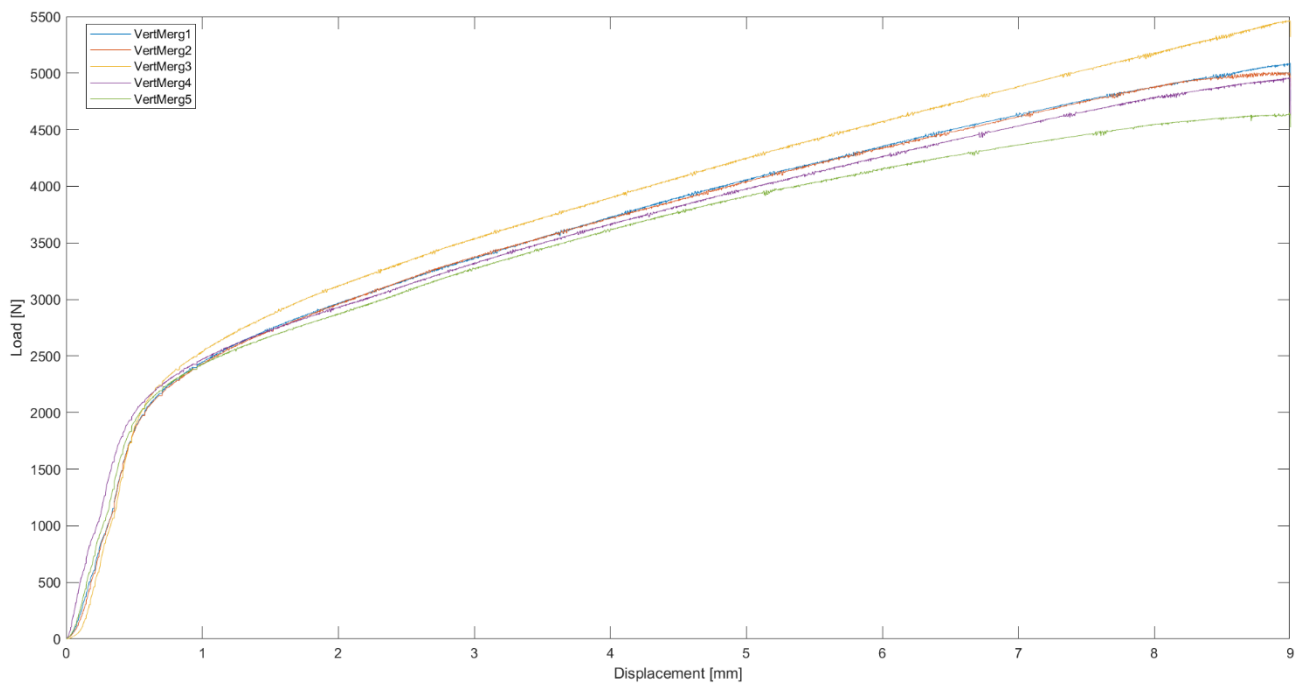


Figure 41 Comparison of the results of the five vertical merged depositions bend test.

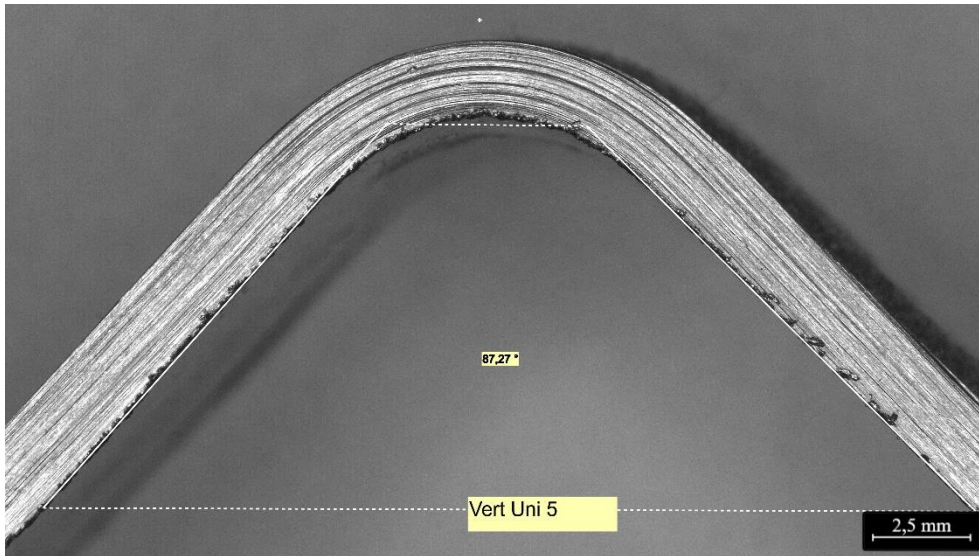


Figure 42 Vertical merged deposition test piece after the bend test. Picture taken with the microscope.

The specimens with vertical separated lines gave rise to virtually the same curves in the force-displacement graph (Figure (42)), with the only exception being sample number 5. The force needed to perform the bend test first rises considerably as the central former has to overcome the initial stiffness of the steel sheet, stiffness that has been increased by the deposition of extra material. Moreover, very minor deformations, caused by the heat induced by the DED machine during the deposition process, likely increased the sample stiffness even further. The change in slope of the curve happens between 0.5 mm and 0.75 mm and this is consistent among all the samples tested, with just some minor differences.

This kind of deposition has resulted in a maximum force exerted by the bending machine of 3390 N for specimen number 5 and between 3743 N and 3863 N for the others. The maximum fibre stresses, computed according to equation number (1) (chapter 3.3), were 1322 MPa for sample number 5, the lowest one, and between 1460 MPa and 1507 MPa for the other ones. Results are reported in Table (6)

Specimen	Maximum load	Maximum fibre stress
/	N	MPa
VertSep1	3772	1471
VertSep2	3863	1507
VertSep3	3826	1492
VertSep4	3743	1460
VertSep5	3390	1322

Mean value	σ	Mean value	σ
3720 N	190 N	1450 MPa	74 MPa

Table 6 Bend test results for the vertical separated deposition test pieces.

Depositing merged tracks on top of the steel sheet resulted in an overall increase of the force exerted by the former to perform the test. The slope change still happens around the same millimetres of displacement, but the force value reached is higher: for example, comparing sample number 3 of both the separated tracks and the merged tracks kind, both at 0.6 mm of displacement, the force exerted increased from 1660 N to 2104 N, a 21.1% increase. The trend after the change in slope is then of a more or less constant increase of force relative to the displacement of the central former, but this slope is higher with respect to that of the separated deposited tracks. In this case, two specimens stand out: number 3 reaches a quite higher maximum load compared to the others, while number 5 a quite lower one. Number 2 through 4 are more consistent among them. This difference might be due to the specimens not being cut or positioned exactly as the others, either inside the DED machine or the bend test machine. All the results of maximum load and maximum fibre stress are reported in table (7). Analysing the mean values for the two set of five samples, the merged lines specimens saw an increase of 35% circa in the maximum load reached during the test.

Both the separated tracks sample and the merged one showed a smaller bending angle than the blank: respectively 84.85° and 87.27°, compared with the theoretical 102.2° and the blank's 90.33°.

Specimen	Maximum load	Maximum fibre stress
/	N	MPa
VertMerg1	5088	1984
VertMerg2	5013	1955
VertMerg3	5467	2132
VertMerg4	4960	1934
VertMerg5	4650	1814

Mean value	σ	Mean value	σ
5036 N	293 N	1964 MPa	114 MPa

Table 7 Bend test results for the vertical merged deposition test pieces.

4.2.4 Horizontal depositions bend test

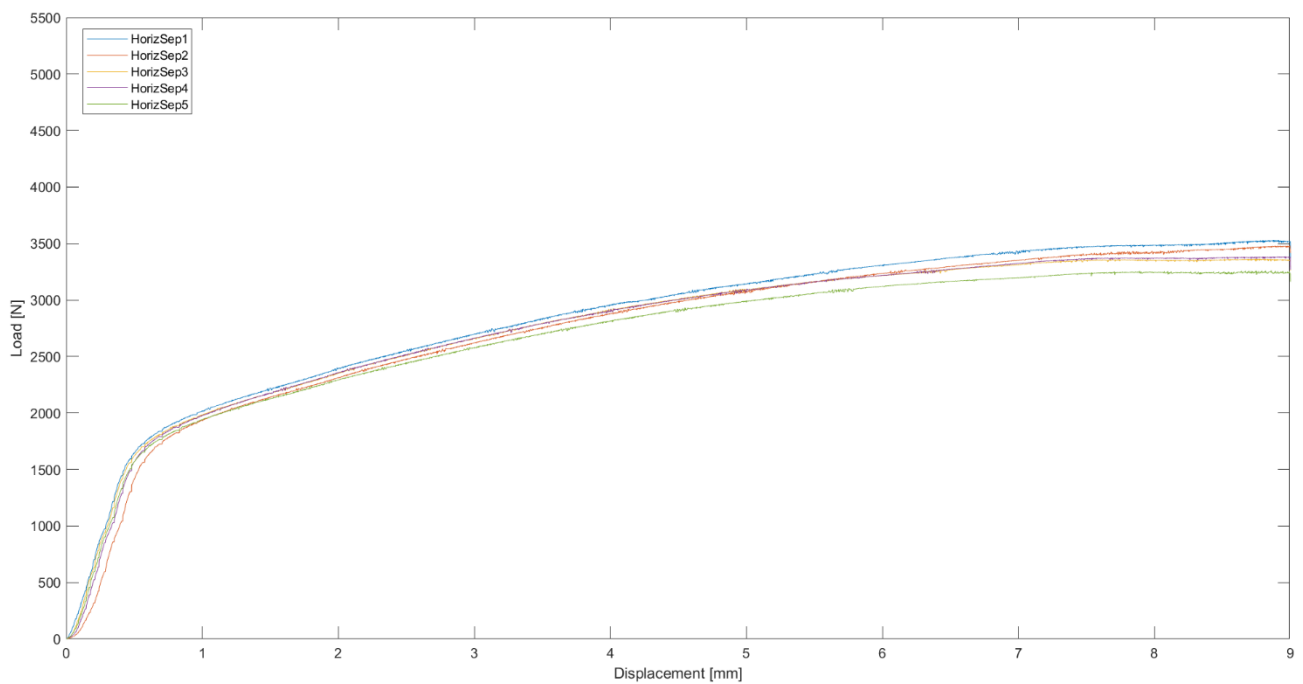


Figure 43 Comparison of the results of the five horizontal separated depositions bend test

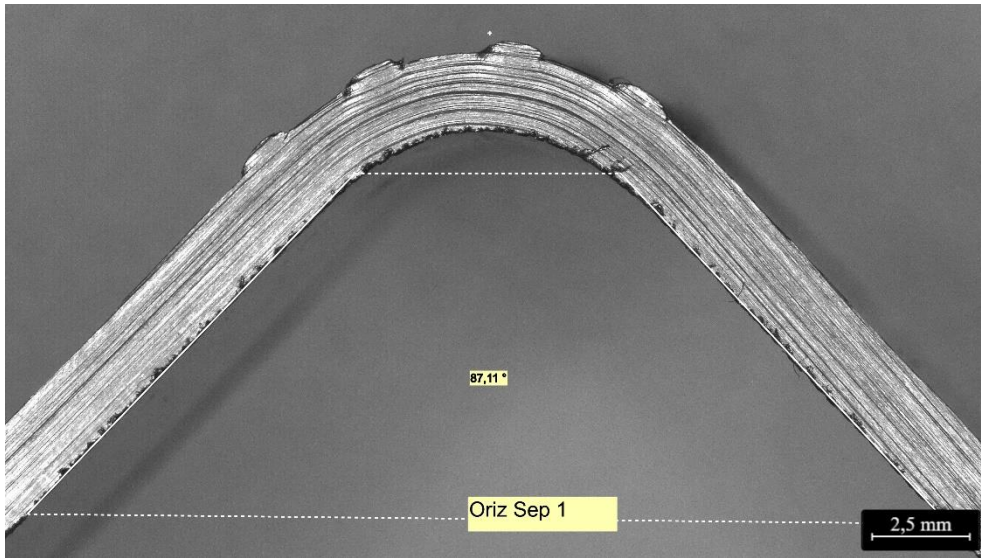


Figure 44 Horizontal separated deposition test piece after the bend test. Picture taken with the microscope.

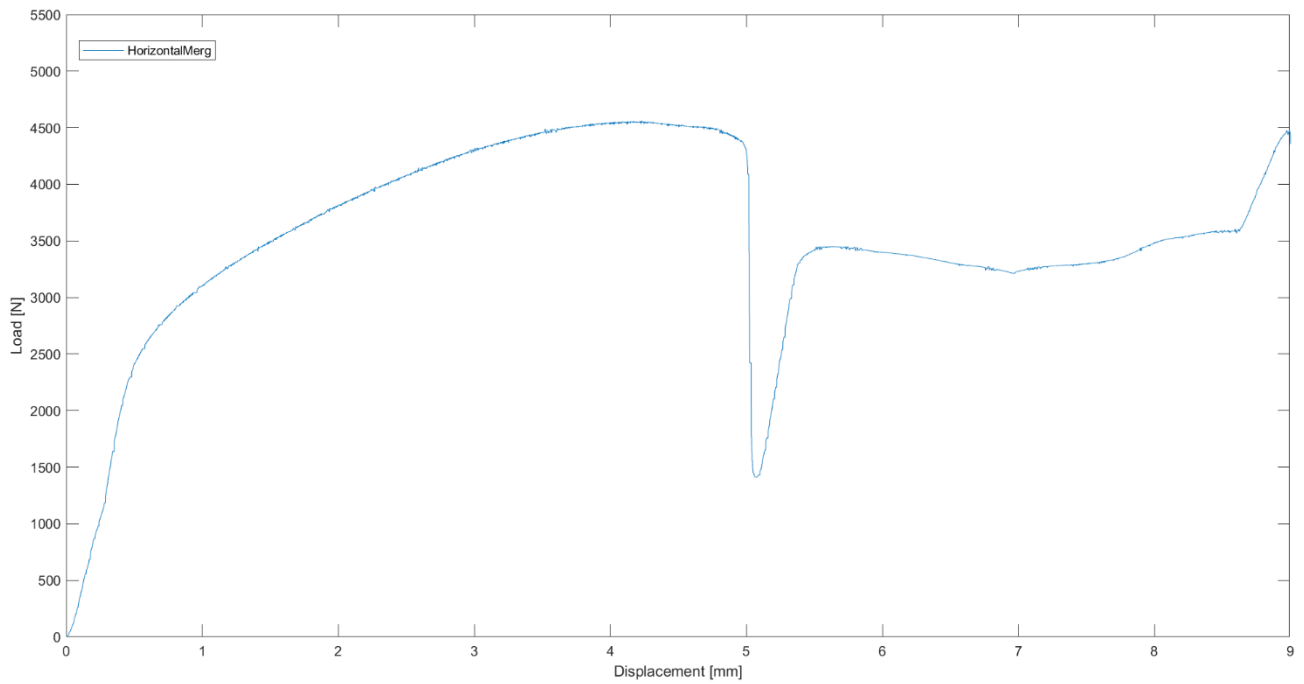


Figure 45 Horizontal merged deposition bend test. The moment of the slip of the test piece is clearly visible.

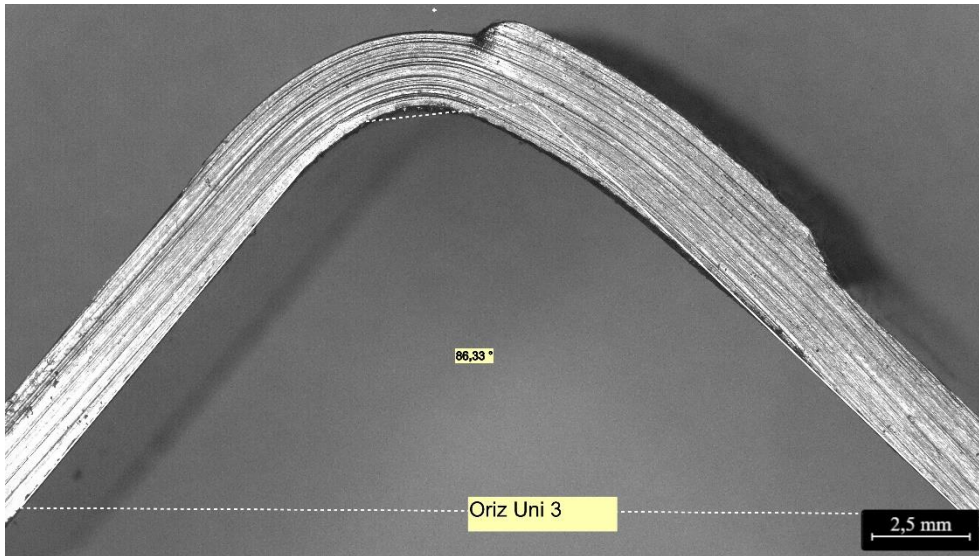


Figure 46 Horizontal merged deposition test piece after the bend test. Picture taken with the microscope.

Like the samples with vertical depositions, also the horizontal separated tracks give rise to two-slope curve, with the change located again between 0.5 mm and 0.75 mm. The discussion will focus only on this kind of horizontal deposition as all the five specimens of merged deposited tracks failed to complete the test correctly. As can be clearly seen in Figure 48, the familiar curve pattern is completely changed once the former reaches around 5 mm of displacement: at this point the sample slips under the increasing load and the test continues with the former acting on a point of the sample next to the deposition. No matter how precise the placement of the samples inside the bend test machine was, the outcome was always the same. To prevent this, we would have needed to increase the section of steel sheet with the deposition, but the premise of this thesis was to perform the test on a constant total deposited strip of 10.5 mm. The results of the bend test for the samples with horizontal merged lines can thus be considered only up to the slip, so prior to 5 mm. The increase in stiffness up to that point was quite high: considering, as done before, the load exerted at 0.6 mm, the value of 1718 N for the separated track climbed to 2621 N, an increase of almost 53%.

Analysing the separated tracks samples, all five tests were very consistent among them, with maximum load reached ranging from 3259 N of sample number 5 and 3528 N of sample number 1. Maximum fibre stress ranged accordingly, from 1271 MPa to 1376 MPa. All the results are reported in table (8).

For what the bending angle is concerned, these specimens were very close to the vertical depositions specimens, so both with a smaller angle than the blank.

Specimen	Maximum load	Maximum fibre stress
/	N	MPa
HorizSep1	3528	1376
HorizSep2	3480	1357
HorizSep3	3363	1312
HorizSep4	3385	1320
HorizSep5	3259	1271

Mean value	σ	Mean value	σ
3403 N	105 N	1327 MPa	41 MPa

Table 8 Bend test results for the horizontal separated deposition test pieces.

4.2.5 Diagonal depositions bend test

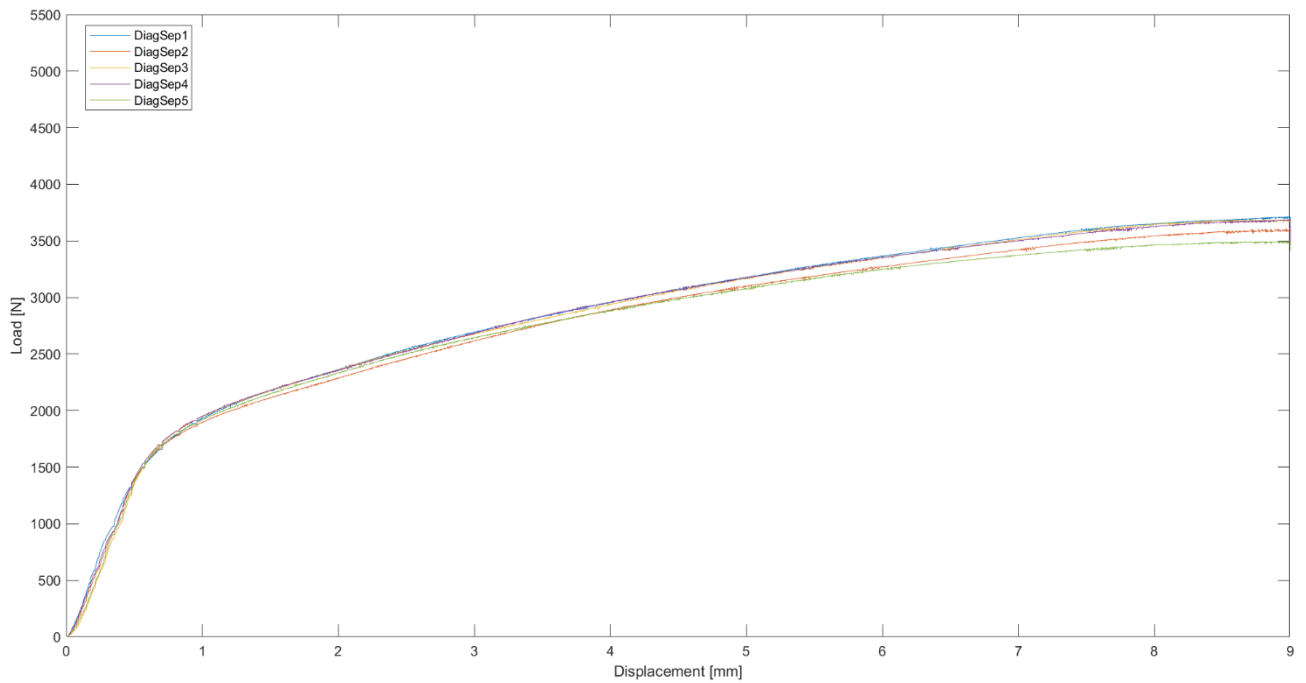


Figure 47 Comparison of the results of the five diagonal separated depositions bend test

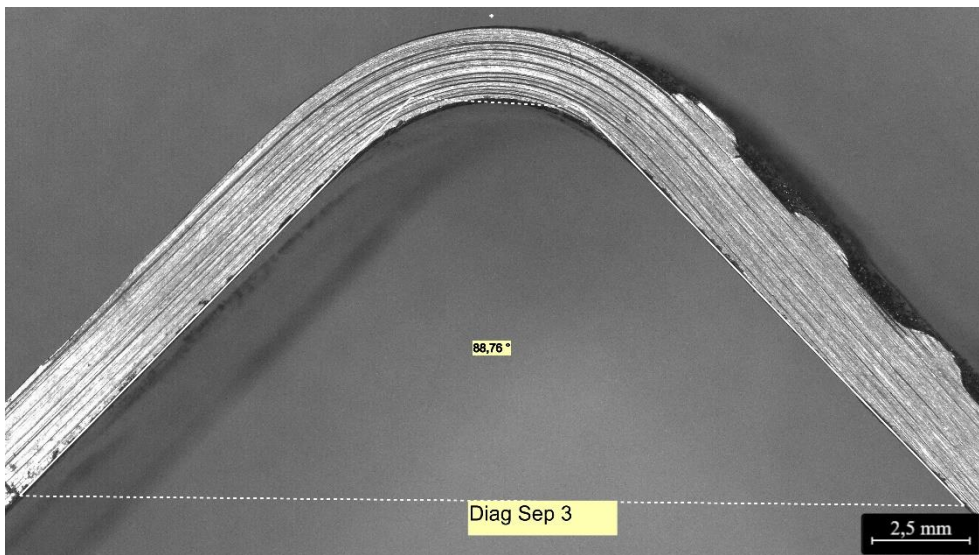


Figure 48 Diagonal separated deposition test piece after the bend test. Picture taken with the microscope.

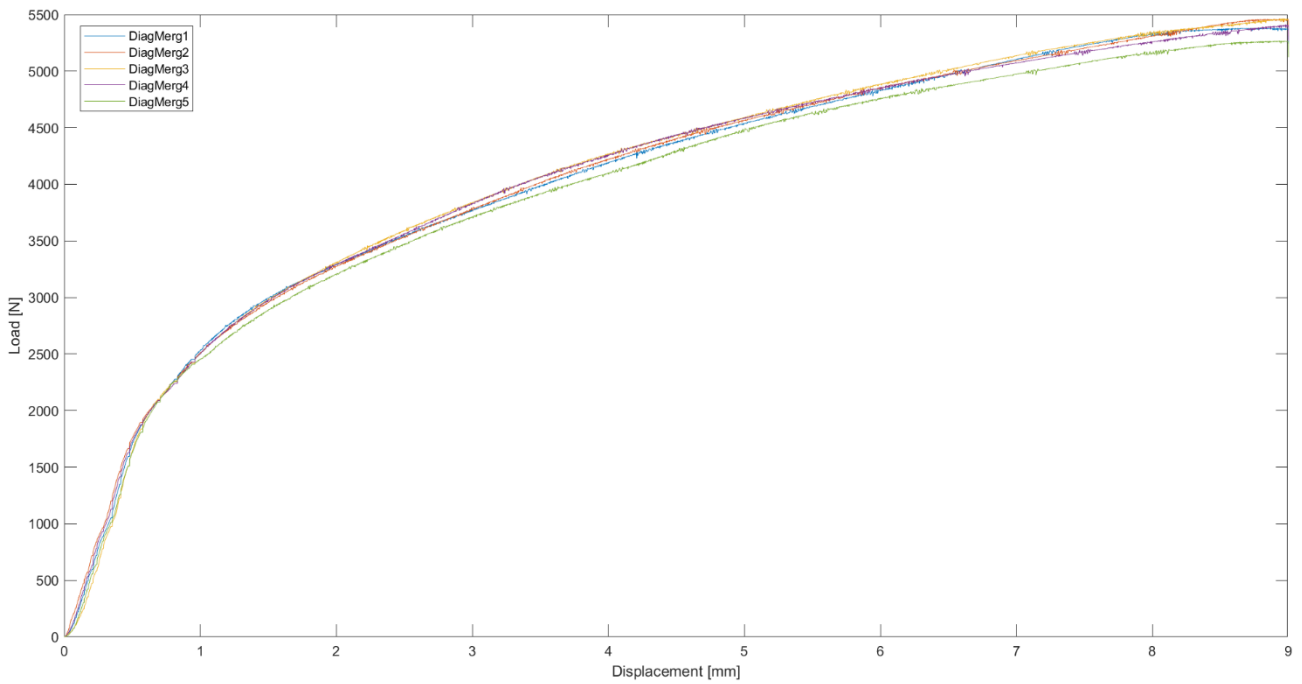


Figure 49 Comparison of the results of the five diagonal merged depositions bend test.

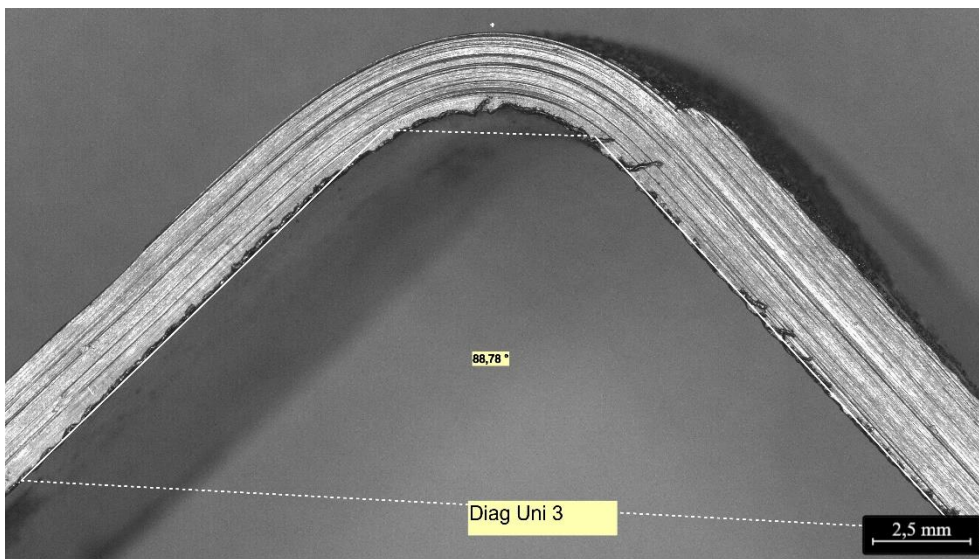


Figure 50 Diagonal merged deposition test piece after the bend test. Picture taken with the microscope.

The behaviour of the samples with diagonal separated tracks was similar to the one of the other deposition strategies, with a clear change in the slope of the curve in the same range of 0.5 mm to

0.75 mm. All the five specimens were fairly close to one another in terms of results and there wasn't much dispersion in the data. The maximum load was reached by sample number 1, at 3715 N, while the lowest was sample number 5, with 3493 N. Maximum fibre stress was in the range 1449 MPa to 1362 MPa. All the results are reported in table (9).

Specimen	Maximum load	Maximum fibre stress
/	N	MPa
DiagSep1	3715	1449
DiagSep2	3607	1407
DiagSep3	3689	1439
DiagSep4	3688	1438
DiagSep5	3493	1362

Mean value	σ	Mean value	σ
3638 N	91 N	1419 MPa	35 MPa

Table 9 Bend test results for the diagonal separated deposition test pieces.

The results of the merged diagonal deposited tracks samples were a bit different from all the others, in the sense that the change of slope of the curves wasn't as drastic, but more gradual. Looking at the same displacement of 0.6 mm, the increase in load is less important than the one observed for the horizontal deposition geometries, growing from 1561 N to 1962 N, an increase of almost 26%.

The absolute highest loads were registered with this category of specimens, with specimen number 3 reaching 5465 N and specimen number 5 being the lowest of the batch, at 5267 N. Maximum fibre stress ranged from 2054 MPa to 2131 MPa. All the results are reported in table (10).

Similar behaviour of the two previous geometries for what the bending angle is concerned: both the merged and the separated tracks depositions showed a smaller angle than the blank. Considering all the different geometries, there wasn't an appreciable difference among them, but every sample showed an increase in the elastic return compared with the blank test.

Specimen	Maximum load	Maximum fibre stress
/	N	MPa
DiagMerg1	5381	2099
DiagMerg2	5462	2130
DiagMerg3	5465	2131
DiagMerg4	5411	2110
DiagMerg5	5267	2054

Mean value	σ	Mean value	σ
5397 N	81 N	2105 MPa	31 MPa

Table 10 Bend test results for the diagonal merged deposition test pieces.

4.2.6 Global comparison

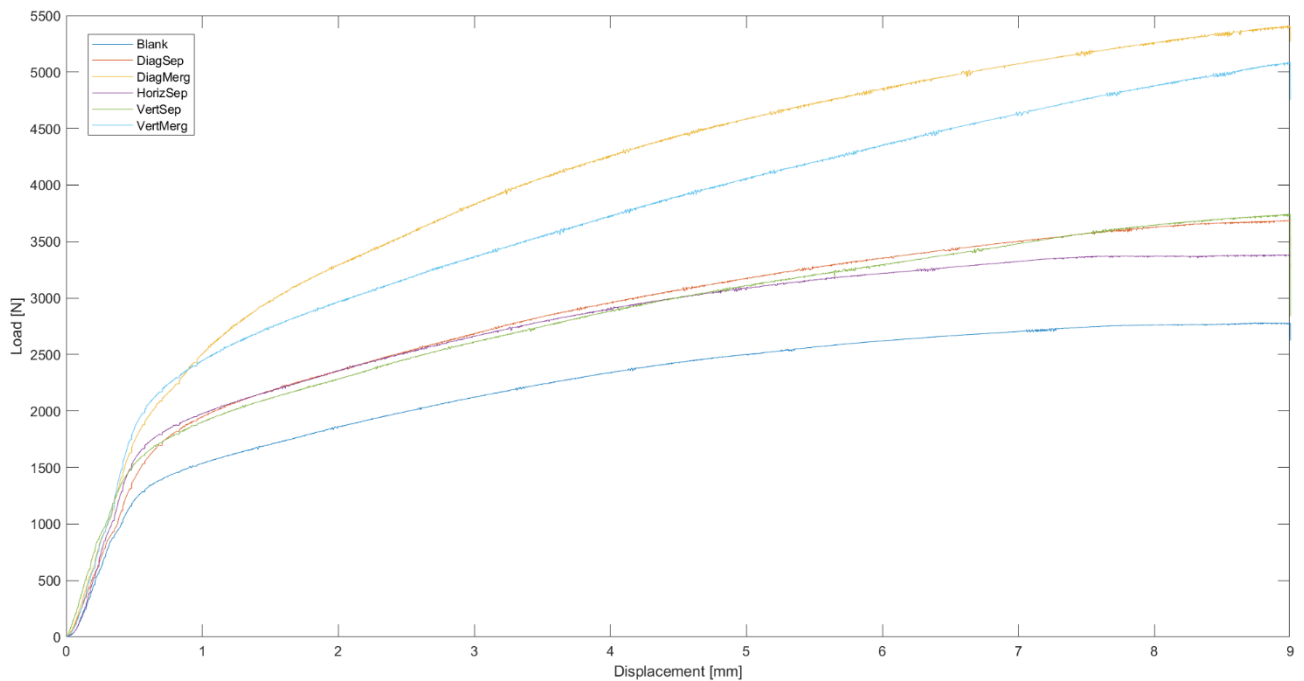


Figure 51 Comparison of the bend test among all the different deposition geometries and the blank.

Different deposition geometries were analysed and compared between the same sample kind, but with the plot in Figure (54) we can have a better understanding of the behaviour of the steel sheets bending after being reinforced in different ways.

Three separate groups can be identified from the plot: the blank sheet at the bottom, with the lowest load across all the test, the middle one composed of the three separated tracks geometries and finally the merged vertical and merged diagonal reinforced sheets, enduring a considerable higher load. What's interesting to notice is how close are all the depositions with the different separated tracks in the plot, instead between the vertical and the diagonal merged samples the difference is quite remarkable. A reason for this could be that the less stiff samples had just a few lines of extra material on top of the substrate steel and that amount of extra material wasn't really helping much in strengthening the steel sheet. The higher load endured compared with the blank sheet is likely only due to the heat cycle the material has been subjected to. When considering the merged geometries, instead, the added steel was enough to make a difference, and that's where we can appreciate the impact the different deposition geometries have on the load withstand by the specimen during the bend test.

Specimen	Maximum load		Maximum fibre stress	
	N		MPa	
DiagMerg	5397	81	2105	31
VertMerg	5036	293	1964	114
VertSep	3719	190	1450	74
DiagSep	3638	91	1419	35
HorizSep	3403	105	1327	41
Blank	2723	107	1062	42

Table 11 Comparison of the average results of the different bend tests.

Even if the samples with the horizontal merged geometry did not complete the bend test due to the slip of the specimen in the machine, it's interesting to notice that up to that point the load those samples were subjected to was the highest overall (Figure (55)). It's not a geometry that adapts

well to different loading characteristics though: even in a controlled test, like the one performed for this thesis, a minor misalignment between the loading point and the deposited strip resulted in the steel sheet bending outside the reinforced zone.

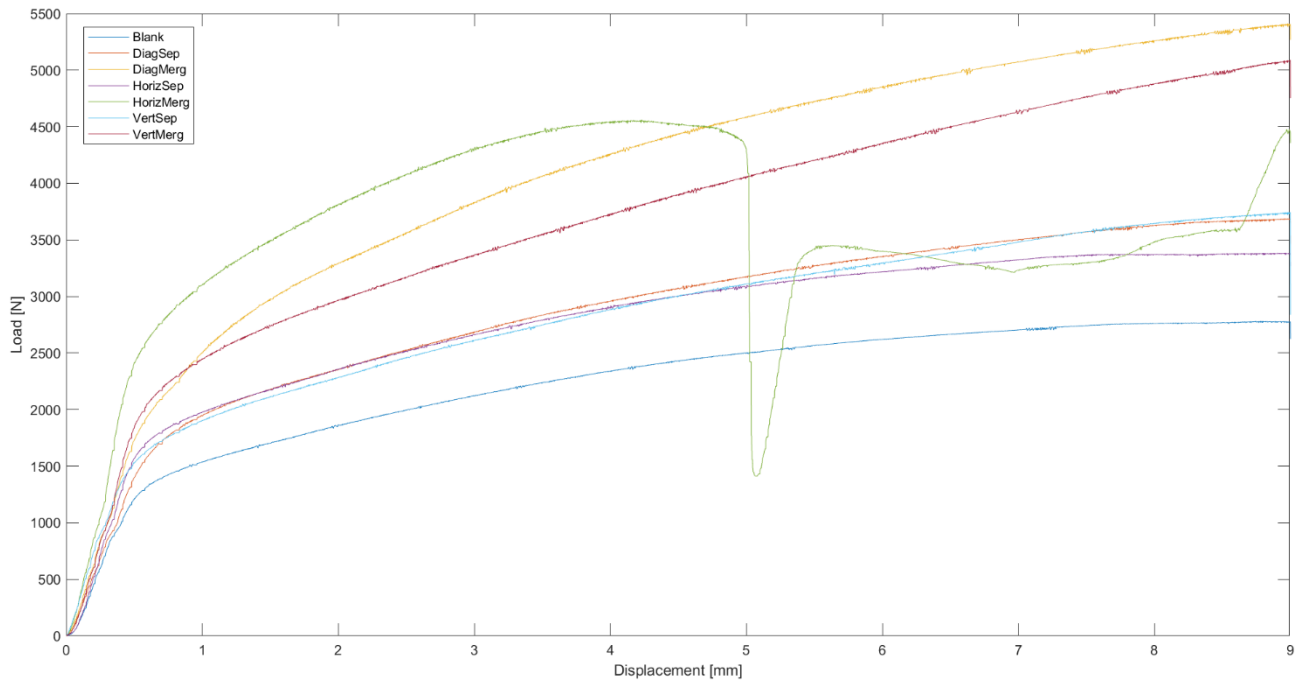


Figure 52 Comparison of the bend test among all the different deposition geometries and the blank. The horizontal merged deposition is included.

5. Conclusions

In this thesis, different reinforcement patterns made by directed energy deposition on a thin steel sheet have been analysed.

The DED machine process parameters have been set according to a series of 9 tests made to identify the best combination of mainly three parameters: the laser power, the powder flow rate and the deposition speed. The laser power couldn't be too high as it would have damaged the steel sheet, but couldn't be too low or the powder would not have received enough energy to properly melt. The flow rate of the powder that was ejected by the nozzle toward the melt pool had to be just right in combination with the other parameters not to have excess powder not being properly melted or not enough of it to form a regular and continuous deposition and a similar thought process was true for the deposition speed.

Once identified, these parameters allowed for a quick and regular series of depositions. A total of 30 samples were produced: 5 with vertical separated tracks, 5 with merged ones, 5 with horizontal separated tracks, 5 with merged ones, 5 with diagonal separated tracks and 5 with merged ones. Finally, 5 blanks without any deposition in order to have a base line to which to compare the other test pieces. The bend test of all these samples was successful in that no cracks could be seen in any part of the rectangular test piece, but the bending of the samples with horizontal merged lines could not be performed in its entirety: once close to 5 mm of former travel, approximately 52° of bending angle, the test piece slipped under the increasing load, finishing the test deforming in a region outside the deposited band. Analysing the results of the other samples, the geometries with separated depositions all had similar curves, with an increase in the maximum load endured of roughly 30% (from ≈ 2700 N reached by the blank test pieces to ≈ 3600 N). The merged depositions showed an even greater increase in the load needed to perform the bend test, with the

diagonal merged geometry reaching the highest value of 5397 N, double that of the blank specimen.

In conclusion, considering future developments, it would be interesting to analyse the behaviour of the different geometries on a larger scale, taking into account different bending axes directions instead of a single fixed reference like it has been done in this thesis.

6. Bibliography

- [1] Saboori, A.; Aversa, A.; Marchese, G.; Biamino, S.; Lombardi, M.; Fino, P. Application of Directed Energy Deposition-Based Additive Manufacturing in Repair. *Appl. Sci.* 2019, *9*, 3316. <https://doi.org/10.3390/app9163316>
- [2] “ASTM F2792-12A, Standard Terminology for Additive Manufacturing Technologies.” ASTM International, West Conshohocken, PA, 2012.
- [3] Wohlers Report 2015, “History of additive manufacturing”, 2015.
- [4] <https://additive-manufacturing-report.com/technology/metal/metal-additive-manufacturing-history/>
- [5] Cattenone A. ,Analysis and Simulation of Additive Manufacturing Process, PhD Dissertation, Università Degli Studi di Pavia, 2018
- [6] <https://www.iso.org/obp/ui/#iso:std:iso-astm:52900:ed-1:v1:en>
- [7] Scott M. Thompson, Linkan Bian, Nima Shamsaei, Aref Yadollahi, An overview of Direct Laser Deposition for additive manufacturing; Part I: Transport phenomena, modeling and diagnostics, Additive manufacturing, Volume 8, 2015, Pages 36-62, ISSN 2214-8604, <https://doi.org/10.1016/j.addma.2015.07.001>
- [8] Nima Shamsaei, Aref Yadollahi, Linkan Bian, Scott M. Thompson, An overview of Direct Laser Deposition for additive manufacturing; Part II: Mechanical behavior, process parameter optimization and control, Additive Manufacturing, Volume 8, 2015, Pages 12-35, ISSN 2214-8604, <https://doi.org/10.1016/j.addma.2015.07.002>
- [9] A.N Chatterjee, Sanjay Kumar, P Saha, P.K Mishra, A.Roy Choudhury, An experimental design approach to selective laser sintering of low carbon steel, Journal of Materials Processing Technology, Volume 136, Issues 1–3, 2003, Pages 151-157, ISSN 0924-0136, [https://doi.org/10.1016/S0924-0136\(03\)00132-8](https://doi.org/10.1016/S0924-0136(03)00132-8)
- [10] Kandice S.B. Ribeiro, Fábio E. Mariani, Reginaldo T. Coelho, A Study of Different Deposition Strategies in Direct Energy Deposition (DED) Processes, Procedia Manufacturing, Volume 48, 2020, Pages 663-670, ISSN 2351-9789, <https://doi.org/10.1016/j.promfg.2020.05.158>
- [11] Kai Zhang, Shijie Wang, Weijun Liu, Xiaofeng Shang, Characterization of stainless steel parts by Laser Metal Deposition Shaping, Materials & Design, Volume 55, 2014, Pages 104-119, ISSN 0261-3069, <https://doi.org/10.1016/j.matdes.2013.09.006>
- [12] A.J. Pinkerton, L. Li, W.S. Lau, Effects of Powder Geometry and Composition in Coaxial Laser Deposition of 316L Steel for Rapid Prototyping, CIRP Annals, Volume 52, Issue 1, 2003, Pages 181-184, ISSN 0007-8506, [https://doi.org/10.1016/S0007-8506\(07\)60560-5](https://doi.org/10.1016/S0007-8506(07)60560-5)
- [13] M. L. Griffith, D. M. Keicher, C. L. Atwood, J. A. Romero, 1. E. Smugeresky*, L. D. Harwell, D. L. Greene, “Free form fabrication of metallic components using LENS”, Sandia National Laboratories Albuquerque, 1996.
- [14] M. Svensson: ‘Ti6Al4 V manufactured with Electron Beam Melting (EBM): mechanical and chemical properties’, in ‘Aeromat 2009’, Dayton, OH, 2009.
- [15] Carter, Luke & Attallah, Moataz & Reed, Roger. (2012). Laser Powder Bed Fabrication of Nickel-Base Superalloys: Influence of Parameters; Characterisation, Quantification and Mitigation of Cracking. 10.1002/9781118516430.ch64.

- [16] Kempen, Karolien & Thijs, Lore & Vrancken, Bey & Buls, Sam & Humbeeck, Jan & Kruth, Jean-Pierre. (2013). Producing crack-free, high density M2 HSS parts by Selective Laser Melting: Pre-heating the baseplate. 24th International SFF Symposium - An Additive Manufacturing Conference, SFF 2013.
- [17] Sames, W.J. & Medina, Francisco & Peter, W.H. & Babu, Sudarsanam & Dehoff, Ryan. (2014). Effect of Process Control and Powder Quality on Inconel 718 Produced Using Electron Beam Melting. 8th International Symposium on Superalloy 718 and Derivatives 2014. 409-423. 10.1002/9781119016854.ch32.
- [18] Mercelis, Peter & Kruth, Jean-Pierre. (2006). Residual stresses in selective laser sintering and selective laser melting. *Rapid Prototyping Journal*. 12. 10.1108/13552540610707013.
- [19] Lu, Xufei & Chiumenti, Michele & Cervera, Miguel & Li, Junjie & Lin, Xin & Ma, Liang & Zhang, Guohao & Liang, Enquan. (2021). Substrate design to minimize residual stresses in Directed Energy Deposition AM processes. *Materials & Design*. 10.1016/j.matdes.2021.109525.
- [20] Ming Tang, P. Chris Pistorius, Jack L. Beuth, Prediction of lack-of-fusion porosity for powder bed fusion, *Additive Manufacturing*, Volume 14, 2017, Pages 39-48, ISSN 2214-8604, <https://doi.org/10.1016/j.addma.2016.12.001>
- [21] Du-Rim Eo, Sun-Hong Park, Jung-Wook Cho, Inclusion evolution in additive manufactured 316L stainless steel by laser metal deposition process, *Materials & Design*, Volume 155, 2018, Pages 212-219, ISSN 0264-1275, <https://doi.org/10.1016/j.matdes.2018.06.001>
- [22] Zhang, Y.N. & Cao, Xinjin & Wanjara, P. & Medraj, Mamoun. (2013). Oxide films in laser additive manufactured Inconel 718. *Acta Materialia*. 61. 6562-6576. 10.1016/j.actamat.2013.07.039.
- [23] Van der Eijk, Casper & Grong, Øystein & Haakonsen, Fredrik & Kolbeinsen, Leiv & Tranell, Gabriella. (2009). Progress in the Development and Use of Grain Refiner Based on Cerium Sulfide or Titanium Compound for Carbon Steel. *Isij International - ISIJ INT*. 49. 1046-1050. 10.2355/isijinternational.49.1046.
- [24] O. Grong, D.K. Matlock, Microstructural development in mild and low-alloy steel weld metals, *Int. Met. Rev.* 31 (1986) 27–48
- [25] REVIE, R. Winston. *Corrosion and corrosion control: an introduction to corrosion science and engineering*. John Wiley & Sons, 2008.
- [26] Module_05_Corrosion_Resistance_of_Stainless_Steels_en, https://www.worldstainless.org/files/issf/Education/English/Module_05_Corrosion_Resistance_of_Stainless_Steels_en.pdf
- [27] F. Kahlen, K. Aravinda, "Tensile Strengths for Laser-Fabricated Parts and Similarity Parameters for Rapid Manufacturing", University of ventral Florida, Orlando, <https://doi.org/10.1115/1.1286472>, 1999.
- [28] Al-Shataif, Yaser & S., Sivasankaran & Al-Mufadi, Fahad & Alaboodi, Abdulaziz & Ammar, Hany. (2019). Manufacturing Methods, Microstructural and Mechanical Properties Evolutions of High-Entropy Alloys: A Review. *Metals and Materials International*. 26. 3. 10.1007/s12540-019-00565-z.
- [29] S. A. K. W. Florian Wirth, «Analysis of melt pool dynamics in laser cladding and direct metal deposition by automated high-speed camera image evaluation» *Additive Manufacturing*, pp. Volume 21-Pages 369-382, 2018.
- [30] De La Batut, Benoit, Omar Fergani, Vegard Brotan, Markus Bambach, and Mohamed El Mansouri. "Analytical and Numerical Temperature Prediction in Direct Metal Deposition of Ti6Al4V." *Journal of manufacturing and Materials Processing* 1.1 (2017)
- [31] W. J. Sames, F. A. List, S. Pannala, R. R. Dehoff & S. S. Babu (2016) The metallurgy and processing science of metal additive manufacturing, *International Materials Reviews*, 61:5, 315-360, DOI: 10.1080/09506608.2015.1116649
- [32] C. Li, Z.Y. Liu, X.Y. Fang, Y.B. Guo, "Residual Stress in Metal Additive Manufacturing", *Procedia CIRP*, Volume 71, 2018, Pages 348-353, ISSN 2212-8271, <https://doi.org/10.1016/j.procir.2018.05.039>

[33] William D. Callister and David G. Rethwisch, "Materials Science and Engineering: An Introduction" 2008. doi: 10.1063/1.2982126.

[34] <https://www.thyssenkrupp-materials.co.uk/stainless-steel-316l-14404.html>

[35] Ziętała, Michał et al. "The Microstructure, Mechanical Properties and Corrosion Resistance of 316 L Stainless Steel Fabricated Using Laser Engineered Net Shaping." *Materials science & engineering. A, Structural materials : properties, microstructure and processing* 677 (2016): 1–10.

[36] ISO 7438:2020.

[37] <https://www.instron.com/en/resources/glossary/m/maximum-fiber-stress>

[38] <https://www.leica-microsystems.com/products/light-microscopes/stereo-microscopes/p/leica-s9-e/>